

A microscopic view of a particle collision, showing a central bright region with radiating lines and a complex, textured pattern of dark and light areas.

Determining DRAGON's acceptance: A Microscopic View

Evan O'Connor, UPEI Physics
August 31st, 2006
DRAGON, TRIUMF

ABSTRACT

DRAGON measures the resonance strengths of nuclear reactions using beams from the ISAC facility, this resonance strength is fundamental in calculating the rates at which elements are created and destroyed in the interior of stars and during explosions like supernovae and novae. A key component of the resonance strength is the yield measurement. For an accurate measurement of the yield, various efficiency fractions must be known including the efficiency of the DRAGON mass spectrometer. This report presents measurements taken with a ^{148}Gd α -source mounted in the gas target of DRAGON, this simulates a reaction with a cone angle of ≈ 20 mrad. A collimator is used that allows a microscopic view of particle transmission in DRAGON. Results suggest that the gas target box axis is lower than the separator axis by ≈ 2 mm, Q1's 'standard' setting is high by $\approx 5\%$, there is a possible quadrupole misalignment between the two electric dipoles of DRAGON which decreases the transmission of particles emitted to the left (looking upstream), and finally there is a possible misalignment that causes a $x - y$ correlation at the final slits. Simulations with GEANT have been performed to test these conclusions with mixed results. Conclusions and recommendations are presented.

CONTENTS

1. Introduction	8
1.1 Elemental Production	8
1.2 Nuclear Astrophysics	10
1.3 DRAGON	11
2. Nuclear Astrophysics and DRAGON	13
2.1 Nuclear Reaction Rates	13
2.2 DRAGON	16
2.3 Gas Target	16
2.4 BGO Array	17
2.5 Electromagnetic Mass Separator	18
2.5.1 Magnetic Multi-poles	20
2.5.2 Magnetic Dipole	21
2.5.3 Electrostatic Dipole	22
2.5.4 Charge and Mass Slits	23
2.6 End Detectors	24
3. Acceptance	26
3.1 Definition of Acceptance	26
3.2 Experimental Setup	28
3.3 Computer Simulations	30

4. Results and Discussion	32
4.1 Source Centered in Gas Target Box	32
4.1.1 Charge Slits	32
4.1.2 Mass Slits	35
4.1.3 Final Slits	37
4.1.4 Conclusions	41
4.2 Source Displaced 2mm up in Target Box	42
4.2.1 Charge Slits	42
4.2.2 Mass Slits	43
4.2.3 Final Slits	44
5. Conclusions and Future Work on Acceptance	47
A. Source Centered in Gas Target Images	50
A.1 Charge Slit Images	50
A.2 Mass Slit Images	53
A.3 Final Slit Images	56
B. Source 2mm high in Gas Target Images	59
B.1 Charge Slits	59
B.2 Final Slits	62
C. Magnetic and Electric Field Settings	65

LIST OF FIGURES

2.1	The Gamow Peak	13
2.2	DRAGON	16
2.3	DRAGON gas target	17
2.4	DRAGON target box	17
2.5	DRAGON BGO array	18
2.6	The electromagnetic components of DRAGON	19
2.7	Quadrupole Doublet	20
2.8	Electrostatic Dipole	22
2.9	Mass Slits	24
2.10	DSSSD, front and back view	25
3.1	Lab frame view of recoiling nucleus	28
3.2	Ray tracings through DRAGON	29
3.3	Collimators used in DRAGON	30
4.1	No collimator, charge slits, source centered	33
4.2	Energy distribution of the ^{148}Gd α source	33
4.3	GEANT simulations of y distribution at the charge slits with the source moved down 2mm and centered	34
4.4	No collimator, mass slits, source centered	36

4.5	GEANT simulation of y distribution at the mass slits with the source moved down 2mm and centered	36
4.6	No collimator, final slits, source centered	38
4.7	GEANT simulation of hit pattern at the final slits with the source moved down 2mm and centered	38
4.8	Stopping distance in DRAGON	40
4.9	No collimator, charge slits, source moved up 2mm	43
4.10	Hole collimator, charge slits, source moved up 2mm and quadrupole 1 at -5% of its nominal value.	44
4.11	No collimator, final slits, source moved up 2mm	45
5.1	Effect on transmission with varying ED2 voltage setting.	49
A.1	Collimator in left orientation, charge slits, source centered	50
A.2	Collimator in right orientation, charge slits, source centered	51
A.3	Collimator in up orientation, charge slits, source centered	51
A.4	Collimator in down orientation, charge slits, source centered	52
A.5	Collimator in hole orientation, charge slits, source centered	52
A.6	Collimator in left orientation, mass slits, source centered	53
A.7	Collimator in right orientation, mass slits, source centered	54
A.8	Collimator in up orientation, mass slits, source centered	54
A.9	Collimator in down orientation, mass slits, source centered	55
A.10	Collimator in hole orientation, mass slits, source centered	55
A.11	Collimator in left orientation, final slits, source centered	56
A.12	Collimator in right orientation, final slits, source centered	57
A.13	Collimator in up orientation, final slits, source centered	57
A.14	Collimator in down orientation, final slits, source centered	58

A.15	Collimator in hole orientation, final slits, source centered	58
B.1	Collimator in left orientation, charge slits, source moved 2mm up	59
B.2	Collimator in right orientation, charge slits, source moved 2mm up	60
B.3	Collimator in up orientation, charge slits, source moved 2mm up	60
B.4	Collimator in down orientation, charge slits, source moved 2mm up	61
B.5	Collimator in hole orientation, charge slits, source moved 2mm up	61
B.6	Collimator in left orientation, final slits, source moved 2mm up	62
B.7	Collimator in right orientation, final slits, source moved 2mm up	63
B.8	Collimator in up orientation, final slits, source moved 2mm up	63
B.9	Collimator in down orientation, final slits, source moved 2mm up	64
B.10	Collimator in hole orientation, final slits, source moved 2mm up	64

LIST OF TABLES

1.1	Main burning stages in stellar interiors	9
4.1	Hit rates observed at the charge slits	35
4.2	Hit rates and transmissions observed at the mass slits	37
4.3	Hit rates and transmissions observed/simulated at the final slits	39
4.4	First-order transfer matrix elements in DRAGON	42
4.5	Hit rates observed at the charge slits with source moved up	44
4.6	Hit rates and transmissions observed at the final slits with source moved up.	46
C.1	Magnetic Field Ratios for Quadrapoles	65
C.2	Current Ratios for Sextupoles	66

CHAPTER 1: INTRODUCTION

1.1 *Elemental Production*

The creation of atoms from their constituents, neutrons and protons, can occur several ways [8]. In the beginning few minutes, protons and neutrons were created from quarks as the universe cooled down. This gave rise to ^1H , and several small Z atoms through fusion, ^2H , ^3He , ^4He and trace amounts of ^6Li and ^7Li . Heavier elements were not produced because the temperature of the universe was cooling too fast to allow further fusion to occur. This type of elemental creation is called big-bang nucleosynthesis.

As the universe further cooled, the first stars were created from this original matter and only inside these stars were heavier atoms first produced. Regular stellar processes can create elements from He to Fe through fusion in the interiors of stars releasing among other things, energy as a by-product. These reactions are exothermic, that is they release energy because, in general, the binding energy of fusion products is less than the sum total of the binding energies of the fusion reactants. ^{62}Ni , ^{56}Fe have the lowest binding energies¹ and therefore fusion above these elements is generally endothermic and requires extra energy to occur. This is called stellar nucleosynthesis.

As temperatures inside stars increase, fusion reactions create heavier and heavier elements starting with He and continuing up to Fe, see Table 1.1 for burning stages and temperatures [7].

¹ ^{62}Ni is not very common relative to ^{56}Fe therefore iron is often quoted as the most stable element.

Hydrogen Burning	60 MK
Helium Burning	230 MK
Carbon Burning	930 MK
Neon Burning	1.7 GK
Oxygen Burning	2.3 GK
Silicon Burning	4.1 GK
Explosive Burning (after supernova)	1.2 - 7.0 GK

Table 1.1: Main burning stages in stellar interiors.

Fusion reactions are not the only reactions that occur in pre-supernova stars. The s-process (slow neutron capture) is in part responsible for creating elements higher than Fe in massive stars up to ^{209}Bi where the s-process can no longer be effective [7]. This process, which occurs in low neutron flux environments, causes nuclei to capture neutrons until the product is unstable, at this time the nucleus will β -decay, increasing the atomic number and returning the nuclei to a stable configuration. This process continues until the ^{209}Bi where a fast α -decay in ^{210}Po prevents further progress.

If the star is massive enough a supernova explosion can give rise to another type of nucleosynthesis: explosive nucleosynthesis. A supernova explosion is the collapse of a stellar core to a neutron star, during this process tremendous energy along with the upper layers of the now destroyed star and many newly created elements past Fe are expelled into interstellar space. The reason elements past Fe can be created in supernova explosions is because there is significant excess energy to allow endothermic fusion to occur. Large neutron flux can also give rise to heavier elements through the r-process (rapid-neutron capture process).

Explosive nucleosynthesis can also occur in novae explosions. A novae explosion typically occurs in a white dwarf binary system. As the companion star progresses into the red giant phase of its life cycle the stellar envelope grows, the outside matter is held lightly to the companion and can be transferred to the surface of the white dwarf. This leads to periodic, rapid burning of the accreted matter. The 'ashes' are either transferred onto the

surface of the white dwarf, increasing its mass, or sent off into the interstellar environment. A recent nova explosion occurred in the constellation of Ophiuchus [5], the star is RS Ophiuchi and has a estimated mass of $1.35 \pm 0.01 M_{\odot}$, very close to maximum limit of white dwarfs. When a white dwarf reaches this limit, a type Ia supernova occurs. Such a supernova, given its close proximity, would provide an excellent opportunity to advance the nuclear astrophysics field. A X-ray burst is similar to a nova with the difference in that the underlying star is a neutron stars instead of a white dwarf. The burning phase of an X-ray burst is much more energetic.

1.2 Nuclear Astrophysics

While the basic evolution of stars is relatively well understood, the rates at which nuclear reactions occur are not so well known. It is essential to know these rates because the abundances of all elements above helium depend on them. For example: The first stage of stellar evolution is hydrogen burning. This process creates He, but since He cannot successfully fuse into ${}^8\text{Be}$ due to ${}^8\text{Be}$ being unstable to α decay with a very short half life, the fusion process stalls at this stage until it becomes hot and dense enough for helium burning to occur at such a rate to create a steady-state population of ${}^8\text{Be}$. At this point, ${}^8\text{Be}$ can fuse with ${}^4\text{He}$ to create ${}^{12}\text{C}$. Since carbon atoms are being created in a helium rich environment, fusion to oxygen (carbon + helium) is also possible. If this reaction (carbon + helium) occurs at a faster rate then $3 {}^4\text{He} \rightarrow {}^{12}\text{C}$ then oxygen is the dominate end product of helium burning because the carbon is converted as soon as it is created. Otherwise, if the reaction happens slower, carbon will be the dominate end product of helium burning. The rates at which new elements are formed, and consequently the rates of destruction of other elements, plays a strong role in determining the lifetime and the composition of stars as well as the make-up of the interstellar environment in the vicinity of

the star. Since C and O are fundamental in the development and sustainment of life these processes and their results are important to understand. These rates can be estimated or constrained by astrophysical observations and grain samples that still exist from pre-solar system times (4.6 billion years ago) but determining actual rates requires other methods.

Nuclear Astrophysics is a branch of physics that deals with the prediction and calculation of nuclear reaction rates in astrophysical environments, mainly stellar interiors but also extreme environments including the surroundings of X-ray bursts, nova and supernova explosions.

1.3 DRAGON

The DRAGON (Detector of Recoils And Gamma Of Nuclear reactions) recoil mass spectrometer at the ISAC (Isotope Separator and Accelerator) facility located at TRIUMF (TRI University Meson Facility) on the University of British Columbia campus in Vancouver BC, Canada is designed to determine, experimentally, very important properties of astrophysically important reactions rates. DRAGON can use both stable nuclei and radioactive nuclei created on-site using either the in-line ion-source connected to the 500 MeV cyclotron of OLIS (Off-Line Ion Source).

DRAGON works by projecting a beam of incoming nuclei onto a gas target, the gas can be either H_2 or He. Nuclear fusion will occur between some of the incoming particles and the gas, this depends on many properties but ultimately on the reaction rate. DRAGON then directs the beam of the particles, and recoils (any products from the fusion process) through an EMS (Electromagnetic Mass Separator) which separates the beam particles from the recoils. The recoils are then detected at the tail of DRAGON. When compared to the incoming beam intensity and several other measurable quantities, important variables

in the reaction rate equation can be determined. More details on DRAGON and the properties of reaction rates it studies can be found in Chapter 2.

DRAGON has studied a number of reactions to date: like the $^{21}\text{Na}(p,\gamma)^{22}\text{Mg}$ [3] and the $^{26g}\text{Al}(p,\gamma)^{27}\text{Si}$ reaction [9], but a common feature to most of these reactions is that they are well within the design limits of DRAGON therefore, all reaction products are fully transmitted through DRAGON. These design limits will be presented in Chapter 2; when reactions approach the design limits of DRAGON it is possible and very likely that all reaction products are not transmitted through DRAGON, instead only a fraction are transmitted. Some very important astrophysical reactions are at the design limit of DRAGON, in order to fully understand what is happening in DRAGON, acceptance studies at DRAGON's limit must be performed. This report outlines and analyzes acceptance studies performed in the Summer of 2006 with DRAGON using an α particle source and various collimators. The methodology of this work is described in Chapter 3 and the results, including a discussion, are presented in Chapter 4. A list of conclusions are included in Chapter 5.

CHAPTER 2: NUCLEAR ASTROPHYSICS AND DRAGON

2.1 Nuclear Reaction Rates

Nuclear fusion reactions occur in stellar environments not because there is significant energy available to overcome the coulomb repulsion of the nuclei, but because there is a non-zero probability of the nuclei tunnelling through the barrier and fusing, only particles with significant thermal energy can achieve this, the relative probability of two particles fusing can be found by simply multiplying the Maxwell energy distribution for particles at a temperature of T with the probability of tunneling through the coulomb barrier, the resulting distribution is called the Gamow Peak and is shown in Figure 2.1, adapted from Reference [7].

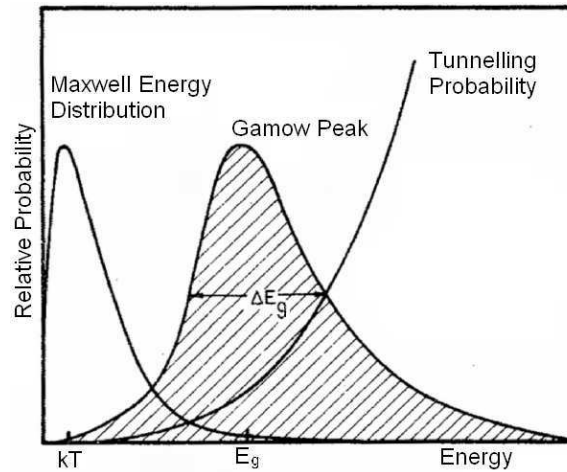


Figure 2.1: Gamow Peak: The Gamow peak represents the probability of nuclear fusion at an energy of E . Figure adapted from [7]

The location of the peak (E_g in Figure 2.1) is dependent on the stellar temperature and the energy of the coulomb barrier, see Equation 2.1,

$$E_g \approx 1.22(Z_1^2 Z_2^2 \mu T_6^2)^{\frac{1}{3}} \text{keV} \quad (2.1)$$

where Z_a is the atomic number of particle a , T_6 is the temperature measured in millions of kelvin, μ is the reduced mass of the nucleons and 1.22 is the result of several fundamental constants such as k , \hbar , e and π .

The Gamow distribution does not, by itself contribute significantly to elemental production, but in reality the majority of stellar nucleosynthesis occurs at a discrete amount of energies where resonances in production occur. Resonances occur in nuclear reactions when the excess energy¹ is equal to an excited state of the product nucleus and is discussed in more detail in Chapter 3. Although, the Gamow distribution is still crucial because resonances occur at many energies, only those with energies near the Gamow peak, $(E_g \pm \frac{\Delta E_g}{2})$, can occur with high probability in stellar environments. Therefore the reaction rate can be written as

$$\langle \sigma v \rangle \approx \left(\frac{2\pi}{\mu kT} \right)^{3/2} \hbar^2 f \sum_i (\omega\gamma)_i \exp\left(-\frac{E_i}{kT}\right) \quad (2.2)$$

where f is a factor to deal with electron screening, $(\omega\gamma)_i$ is referred to as the resonance strength of resonance i centered at an energy of E_i . Again, μ is the reduced mass of the two particles. The sum is taken over all resonances that occur near the Gamow energy.

The resonance strength of a given reaction can be determined by finding the thick target yield², the form is shown in Equation 2.3,

¹ excess energy consists of the energy equivalent of excess rest mass and also any excess kinetic energy.

² This assumes that the resonance width is narrow, see more details in Reference [7] for thick resonances or thin targets.

$$\omega\gamma = Y_{\infty} \frac{2}{\lambda^2} \frac{M\varepsilon}{M+m} \quad (2.3)$$

where λ is the deBroglie wavelength ($\sqrt{h^2/2\mu E_{cm}}$), ε is the stopping cross section of the target which is equal to the energy loss per unit area density ($\text{eV atoms}^{-1} \text{ cm}^2$), M is the mass of the target particle, m is the mass of the beam particle and Y_{∞} is the thick target yield measured experimentally as

$$Y_{\infty} = \frac{\text{Recoils detected}}{(\text{Incident beam particles}) \times (\text{Charge state fraction}) \times (\text{II Detector efficiencies})} \quad (2.4)$$

where $\langle \text{Recoils detected} \rangle$ is the number of reaction products detected in DRAGON, $\langle \text{Incident beam particles} \rangle$ is the number of beam particles that passed through the target and $\langle \text{Charge state fraction} \rangle$ is the fraction of recoils that have the charge selected in DRAGON³. Finally, $\langle \text{Detector efficiencies} \rangle$ are various correction factors assigned due to the detectors used in DRAGON; for example the DSSSD, γ -ray array, and the recoil spectrometer. It is the last one that this report focuses on.

DRAGON can determine these quantities (Equation 2.4) to calculate the yield as well as the stopping power of the target through various detectors and techniques, this then allows for the calculation of resonance strengths and energies and then ultimately contribute to reaction rate calculations.

³ DRAGON can only detect one charge state at a time but recoils are distributed over many charge states, see Section 2.5.2 or [11] for more details.

2.2 DRAGON

As an apparatus, DRAGON consists of 4 main sections: a gas target, a BGO (Bismuth Germinate Oxide) γ -ray detector array, an electromagnetic mass separator, and end detectors. These four sections are used together to both perform nuclear reactions and detect them, each is explained in this chapter; a layout of DRAGON is shown in Figure 2.2.



Figure 2.2: DRAGON

2.3 Gas Target

The ISAC facility can produce many different beams of heavy ions at moderate energies (0.15-1.7 MeV/amu). These ions are directed to the DRAGON which consists of a windowless gas target approximately 12 cm in column length, for a graphical description

of the gas target and the differential pumping used to maintain a vacuum around the gas target see Figure 2.3, a more detailed view of the target box is shown in Figure 2.4.

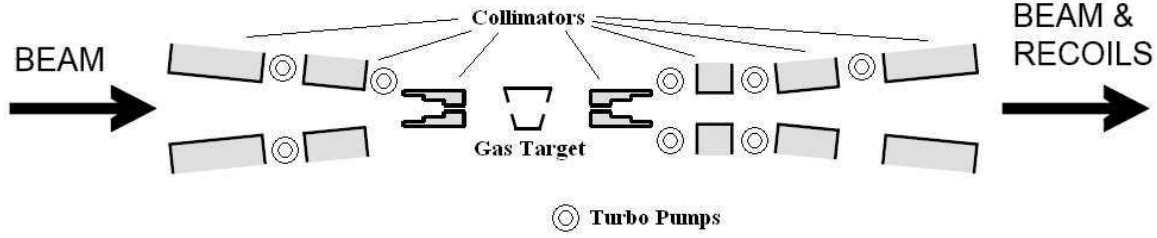


Figure 2.3: The DRAGON gas target: Included is the windowless gas box, collimators to restrict gas flow and turbo pumps to maintain vacuum away from the gas target. Five Roots blowers and one roughing pump are positioned in the gas target area as well to aid in the differential pumping.

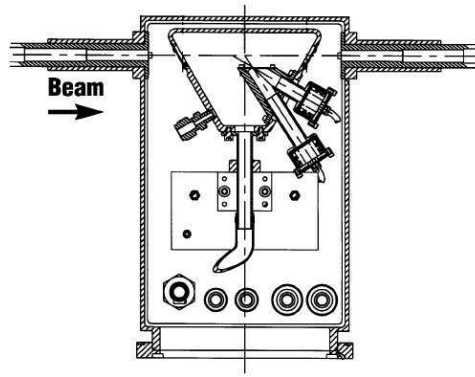


Figure 2.4: The DRAGON target box: The beam enters from the left and interacts with the gas in the trapezoidal container, outside the container the gas pressure is quickly reduced by orders of magnitude by the Roots blowers and turbo pumps.

2.4 BGO Array

During resonance reactions (Section 3.1) the heavy nuclei fuse with a proton or an α particle leaving the recoil in an excited state. For the reactions being studied with DRAGON, the excited recoil quickly decays by emitting one or more γ -rays. These γ -rays are detected, along with their energy, with an array of γ -ray detectors. The elements are made

from Bismuth Germanium Oxide which is a high Z , dense material that has very little afterglow (quick reaction time). The array consists of 30 of these detectors arranged so that they cover as much of the solid angle as possible⁴. The BGO array is shown in Figure 2.5.

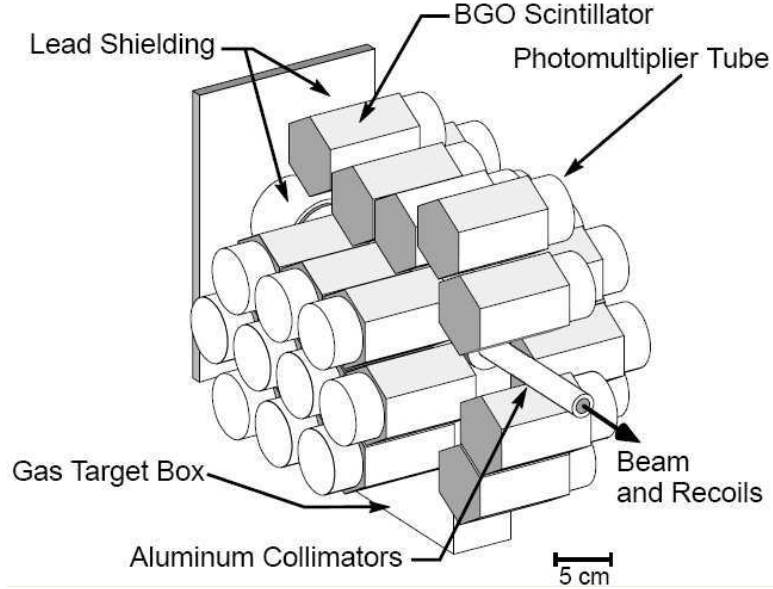


Figure 2.5: The DRAGON BGO array: The detectors are arranged around the target box to detect the γ -rays coming from the de-excitation process of the nuclei in the target box.

2.5 Electromagnetic Mass Separator

Once the recoils have been created in the gas target, they must be separated from the rest of the beam particles in order to be counted and hence determine the yield. This process must be done accurately because for some reactions, there can be only 1 recoil for every 10^{11} beam particles. A schematic of the DRAGON electromagnetic mass separator (EMS) shown in Figure 2.2, a more detailed description is shown in Figure 2.6.

⁴ Detector cannot be placed along the beam line or below the target box as they would obstruct the beam line and vacuum system respectively.

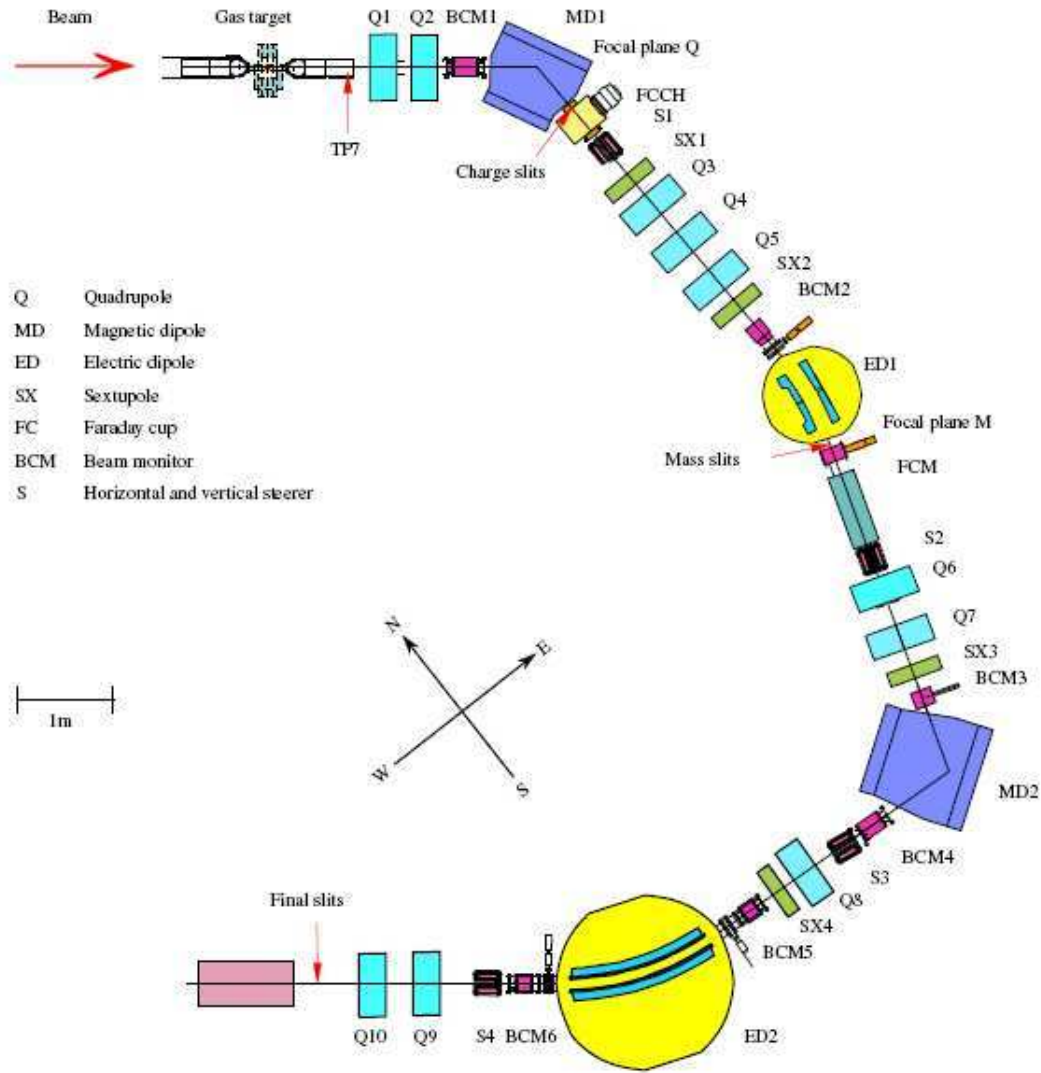


Figure 2.6: The electromagnetic components of DRAGON: The gas target and the BGO array are located at the head of DRAGON, the rest of DRAGON is the EMS.

The DRAGON EMS is divided into 2 main parts, each doing effectively the same thing by separating the beam of particles by the charge to mass ratio, because of this only the first half of the separator needs to be explained in detail beginning with the magnetic multi-poles.

2.5.1 Magnetic Multi-poles

Multi-poles, are electromagnetic elements that focus and de-focus charged particle beams. The simplest case of a multi-pole is a quadrupole which acts identical to a thin lens with the exception that instead of focusing or defocusing an entire beam, a quadrupole focuses in one direction (horizontal or vertical) and de-focuses in the other (vertical or horizontal). In order to focus a beam to a point two quadrupoles are needed, this is called a quadrupole doublet and is shown in Figure 2.7.

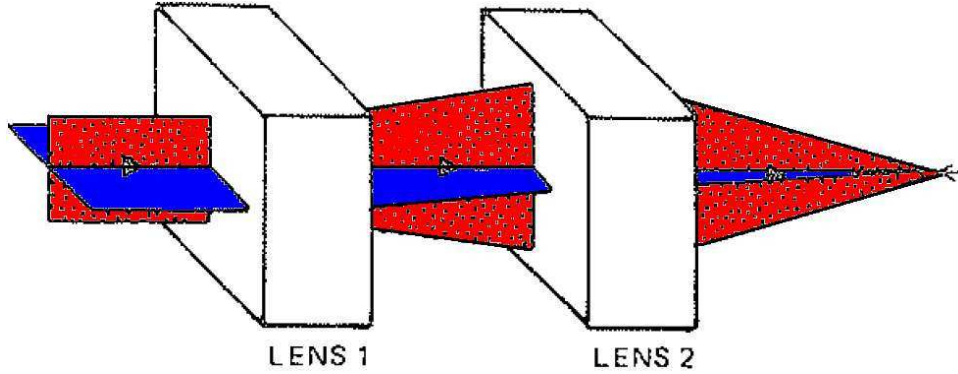


Figure 2.7: Quadrupole doublet, the first element focuses in the horizontal plane and de-focuses in the vertical plane, the second element does the opposite, the beam comes to a focus further along the beam axis. Figure adapted from [7].

DRAGON has three doublets, one triplet⁵, and one single quadrupole. Higher order multi-poles are used in DRAGON (four sextupole) to correct second order terms that appear in the beam along the beam axis, these are not described here but arise due to finite beam spot at the source, energy deviations, etc. One of DRAGON's quadrupoles is designed to have a sextupole element, this as well is used to reduce higher order terms and is used to save both space and production cost.

⁵ Similar effect as a doublet but allows for a more versatile focus (adjustable magnification and focal length).

2.5.2 Magnetic Dipole

The beam of incoming particles from ISAC is in a constant charge state; as the beam passes through the gas in the target, the charge state evolves due to electrons being picked up from or lost to the gas. Due to this fact, the particles coming out of the target are distributed in charge. The distribution depends on the pressure, energy, charge-changing cross sections and the type of target particle. DRAGON can only transmit one charge state for detection since the field strengths depend on q , therefore DRAGON has magnetic dipoles (MDs) to separate momentum-to-charge states. For more information of charge state distributions see [11].

If a particle is traveling in a magnetic field that is perpendicular to the direction of travel then the particle will feel a force in the other perpendicular direction. This is described through Equation 2.5 and gives rise to circular motion.

$$\vec{F}_B = q\vec{v} \times \vec{B}, \quad (2.5)$$

where \vec{F}_B is the force exerted on the particle, q is the charge, \vec{v} is the velocity of the particle, and \vec{B} is the magnetic field. Equating the magnitude to the centripetal force,

$$m\frac{v^2}{r_c} = q|\vec{v} \times \vec{B}| = qvB, \quad (2.6)$$

where the cross product's *sin* term vanishes because directions are perpendicular and isolating q , Equation 2.6 becomes

$$B = \frac{1}{r_c} \frac{p}{q}, \quad (2.7)$$

Here a choice of magnetic field chooses a momentum-to-charge ratio since r_c is constant, all unwanted ratios are eliminated by the charge slits because they have different radii of curvature, see Section 2.5.4.

2.5.3 Electrostatic Dipole

The other main suppression elements in DRAGON are the electrostatic dipoles (ED1 and ED2). These elements are located after MD1 and MD2 respectively, one of DRAGON's EDs is shown in Figure 2.8. The red elements are electrodes, the larger radius electrode (outside) is positively charged and the inner electrode is negatively charged so that an electric field is present between the two plates. The curvature of the electrodes causes the particles to travel with a circular trajectory, by equating the force of the electric field with the centripetal force (Equation 2.8), the relation between the electric field and energy becomes apparent.

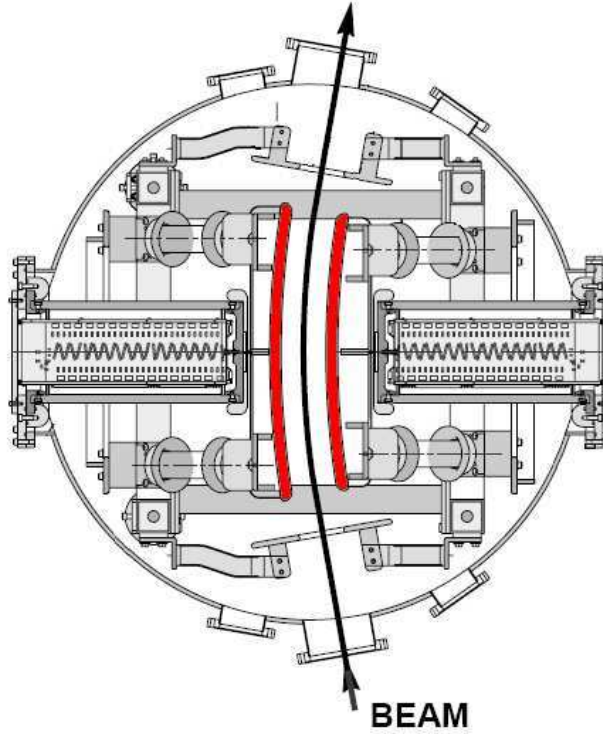


Figure 2.8: An electrostatic dipole: This element is responsible for separating particles of different energy-to-charge ratios.

$$qE = m \frac{v^2}{r_c} = \frac{2E_{recoil}}{r_c}, \quad (2.8)$$

where q is the charge of the particle, E is the electric field strength between the electrodes, m is the mass of the particles, v is the velocity of the particles, r_c is the radius of curvature of the dipole defined as the arithmetic average of the electrodes' radius of curvature, and E_{recoil} is the kinetic energy of the recoil.. Upon rearrangement, this becomes

$$E = \frac{2E_{recoil}}{qr_c}, \quad (2.9)$$

since the radius of curvature is a design feature of the dipoles, an electric field can be chosen such that the desired particle energy-to-charge ratio is transported through DRAGON. Particles of different energy-to-charge ratios progress through the dipoles at different radii of curvature, these unwanted energies are stopped at the mass slits, see Section 2.5.4. The DRAGON recoil spectrometer is special because the particles of interest, theoretically, all have the same momentum, therefore the MDs separate by charge and then, since the charge is the same for all particles, the EDs separate by mass.

2.5.4 Charge and Mass Slits

DRAGON is designed so that particles of interest (correct charge state q and mass m) are transmitted through DRAGON but also that at three⁶ locations the envelope of particles is at a focus. These three locations are immediately after the first MD (charge focus), immediately after the first ED (mass focus) and at the tail of DRAGON (final focus). Narrow slits are then used to stop unwanted states (charge states at the charge focus and mass states at the mass focus) while allowing the selected state to continue on in the separator. The charge and mass slits are the main method of beam suppression, so the foci must be accurate and as small as possible. This is illustrated in Figure 2.9 for the mass slits.

⁶ Another focus exists in DRAGON after the second MD, but no slits are present at this location.

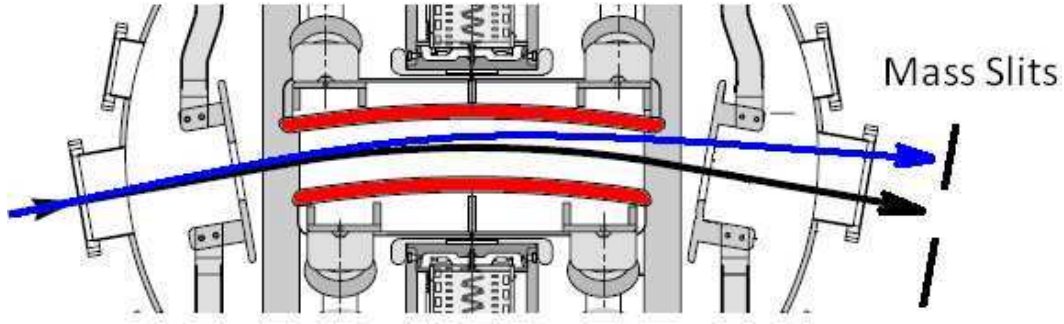


Figure 2.9: Mass Slits: The upper (blue) trajectory corresponds to that of particles with a smaller mass. The radius of curvature is larger, therefore these particles are not transmitted through the mass slits but rather stopped on them.

Since the particles are at a focus this makes these areas ideal for placing detectors to monitor the beam or recoils, more on this technique will be discussed in Chapter 3.2

2.6 End Detectors

DRAGON has several end detectors, each has both advantages and disadvantages. This work only uses one of the detectors, namely the double-sided silicon strip detector (DSSSD), this is described below. The other detectors are an ion chamber and an electrostatic mirror, foil and MCP combination.

A DSSSD consists of two planes of silicon strips placed on either side of a Si wafer. One set of strips are vertical (giving horizontal position information) and one set are horizontal (giving vertical position information). Together these planes give a 16x16 pixelated picture of the beam envelope at the location of the detector. Each strip is 3mm wide and 48 mm in length. The DSSSD can also accurately determine the energy of the incident particle. This detector has an efficiency of $\approx 96\%$ which arises from the geometric coverage of the silicon strips in the 48mm \times 48mm detector area. The DSSSD is cooled to -10°C and uses a bias voltage of 70V to decrease the noise. A picture of a DSSSD detector is shown in Figure 2.10.



Figure 2.10: DSSSD, front and back view.

CHAPTER 3: ACCEPTANCE

3.1 Definition of Acceptance

Before describing the design limits of DRAGON, it is necessary to describe the nuclear reaction process in the gas target in more detail. For purposes of explanation, the reaction $^{12}\text{C}(\alpha, \gamma)^{16}\text{O}$ is used. It is useful to use this reaction both because of its astrophysical importance and because it is at the design limit of DRAGON at certain energies. The incoming carbon atom interacts with a helium nucleus (at rest), if a fusion event occurs then the resulting product is oxygen. Using conservation of momentum, the final velocity (and kinetic energy) before the emission of the γ -ray(s) can be calculated.

$$v_{f,O^*} = \frac{m_C}{m_O} v_{i,C} \quad (3.1)$$

$$E_{f,O^*} = \frac{1}{2} m_O^* v_{f,O^*}^2 = \frac{1}{2} m_O^* \left[\frac{m_C^2}{m_O^2} v_{i,C}^2 \right] \approx \frac{3}{4} E_{i,C} \quad (3.2)$$

where m_C is the mass of carbon and m_O is the mass of oxygen, for this calculation, 12 and 16 amu respectively are sufficient.

The rest mass of a carbon atom is 12.0 amu, whereas the rest mass of an α particle is 4.002603. After fusion the rest mass of oxygen is 15.994915, the mass difference between these reactants and products is 7.68863×10^{-3} amu which results in an excess energy of 7.115763 MeV. Using this and the excess energy from Equation 3.2 ($1/4 E_{i,C}$) we note the excess energy is,

$$E_{excess} = \frac{1}{4}E_{i,C} + 7.116\text{MeV} \quad (3.3)$$

if this energy, E_{excess} , is equal to an excited state of oxygen then a resonance occurs in oxygen production [7]. The excited state will release this energy as a γ -ray or cascade of γ -rays; it is the de-excitation of the recoil particle that determines whether or not DRAGON can fully measure the yield. If the γ -ray's momentum has a component in a direction perpendicular to the beam axis then the recoil will be 'kicked' off axis in the other direction to conserve momentum. If the γ -ray's momentum is completely perpendicular to the beam axis then the recoil will receive the largest kick¹. This kick will have a momentum of $\frac{E_\gamma}{c}$, therefore the recoil's new off-axis velocity is

$$v_{off-axis,O} = \frac{E_\gamma}{cm_O} \quad (3.4)$$

therefore the angle in the lab frame of the recoil particle is simply the arc-tangent of the two velocities, see Figure 3.1 for geometric definition in the lab frame.

$$\theta_{off-axis,O} = \arctan \left(\frac{E_\gamma}{c m_O \sqrt{\frac{2E_O}{m_O}}} \right) \quad (3.5)$$

For $^{12}\text{C}(\alpha,\gamma)^{16}\text{O}$ with a carbon beam energy of 12.84 MeV, the maximum recoil angle is 17.9 mrad. DRAGON was designed such that any recoil particle with a recoil angle of less than ≈ 20 mrad would be fully transmitted through. This report investigates what happens to recoil particles created in the gas target that have recoil angles between 0 mrad and DRAGON's limit. Also of importance is how well computer simulations can reproduce experiments at large recoil angles. This is important because the only way to

¹ There is a subtlety here where the largest kick actually occurs when the γ -ray is emitted $90^\circ - \theta$ from the beam axis, where θ is shown in Figure 3.1. This derivation also ignores relativistic effects which is valid for energy studies at DRAGON.

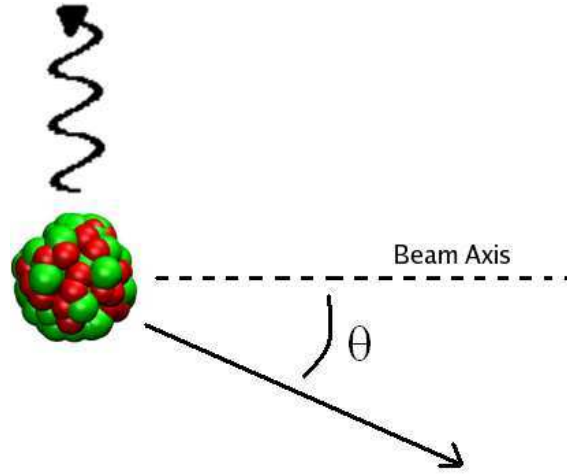


Figure 3.1: Lab frame view of recoiling nucleus assuming that the γ -ray is emitted perpendicular to the beam axis.

obtain an accurate DRAGON efficiency fraction (used in the yield equation) is to simulate each reaction and determine the fraction of particles lost.

Figure 3.2 shows a computer simulation of particle trajectories traveling through DRAGON. As the particles are emitted from the target at larger angles the path through DRAGON becomes 'unstable' and particle loss can become high. For example, The x envelope approaches the beam pipe in the quadrupole triplet.

3.2 Experimental Setup

A Gadolinium (^{148}Gd) α source with an activity of $\approx 3 \times 10^5$ Bq is placed in the centre of the DRAGON gas target. While α particles are emitted in all directions, the pumping system of the gas target stops all α particles except those emitted within ≈ 20 mrad of the beam axis looking downstream. The distribution of α particles entering into the EMS are comparable to a reaction with a cone angle of ≈ 20 mrad. In addition to letting all α particles into the EMS, collimators are used to further restrict the distribution. This allows for a 'microscopic' look at how DRAGON transmits charged particles. There are

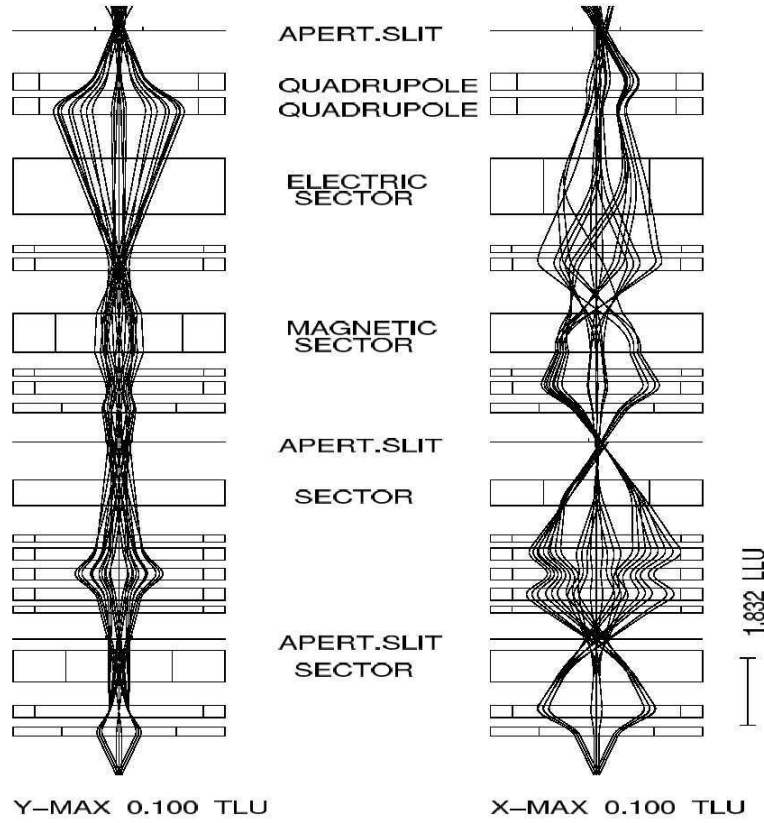


Figure 3.2: Ray tracings of ^{19}Ne recoils through DRAGON, particles begin on the bottom and progress through DRAGON. In each direction (x and y), three sets of rays are shown with initial angles of -16.5 mrad, 0 mrad, and 16.5 mrad each set of rays contains three initial positions (centre of gas target and ± 2.5 mm). For each combination of these values, the energy of the recoils is 4.033 MeV, and $\pm 3\%$.

five restrictive collimators, shown in Figure 3.3. Collimators are labeled as viewed looking upstream at the collimator². For the left (looking upstream) collimator, the vertical angle range assuming a particle is emitted from the centre of the gas target is -5.7 mrad to $+5.7$ mrad. The horizontal angle range is from -7.1 mrad to -22.1 mrad. Other collimator angles can be extracted from these. For the hole collimator, the radial angle range is 0.0 mrad to 6.8 mrad.

The DSSSD is cooled to -10°C and set with a bias voltage of 70V . The three focus

² Most optics codes use downstream as the descriptive direction, upstream is used in this report to denote collimator positions only.

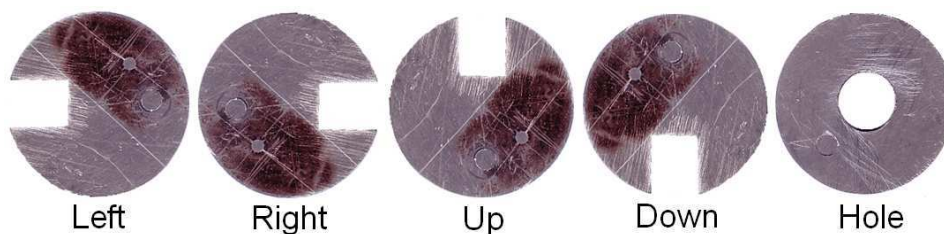


Figure 3.3: Collimators used in DRAGON, Collimators are labeled as viewed looking upstream at the collimator

points of DRAGON are ideal for observing the shape and intensity of the α particles because the beam cross section is small, the detector can be mounted directly after³ the focus point.

The combination of six collimator positions (including the lack of collimator position) and three detectors gives a total of 18 measurements for one set. Along with the nominal settings, other measurements were made: energy mistunes (2 sets), slight changes in quadrupole strengths (1 set), source position movements (1 set), and a combination of all four giving a total of 249 measurements comprising this report.

3.3 Computer Simulations

For some measurements, computer simulations have been performed to simulate the beam shape at the detector locations and particle losses throughout DRAGON. Computer simulations can be used to some extent as a diagnostic to probe problems in reality. The simulation program GEANT is used to calculate the particle trajectories through matter, electric fields and magnetic fields, it was developed at CERN, more information on GEANT and DRAGON's version of GEANT can be found in References [2; 1; 10]. The previous DRAGON GEANT simulation was upgraded to include a more realistic representation of

³ At the final focus the detector is $\approx 66\text{cm}$ behind the focus point, this is acceptable because the beam is still within the detector region at this point.

the DRAGON separator as well as built in collimator support features. Updated versions of the DRAGON GEANT code can be found in the DRAGON CVS.

CHAPTER 4: RESULTS AND DISCUSSION

This chapter is divided into several sections, the first section contains data and simulations with the α source centered in the gas target box. As a result of this data the source was moved up 2mm. This data is presented in the second section. In each section, data is presented for the different detector locations (mass slits, charge slits, and final slits) along with a discussion and implications of the data. All slits were opened completely in all the runs performed in this report. Standard settings for all magnetic and electric elements are given in Appendix C.

4.1 Source Centered in Gas Target Box

4.1.1 Charge Slits

Figures A.1 through A.5 show the observed hit patterns at the charge slits, along with the x and y projections for all five collimator positions, these images appear in Appendix A. Positive x -values on the DSSSD chip are closest to the outer edge of DRAGON. Positive y -values are above the beam axis. The measurement where no collimator was used is shown in Figure 4.1.

There are three interesting properties of the hit pattern in Figure 4.1: (a) there is a tail extending into the negative x zone, and (b) the centroid of the y distribution is offset by ≈ 5 -6 mm in the positive y direction. The tail in the x hit pattern is due to bending properties of the magnetic dipole. The α source is not mono-energetic but rather follows

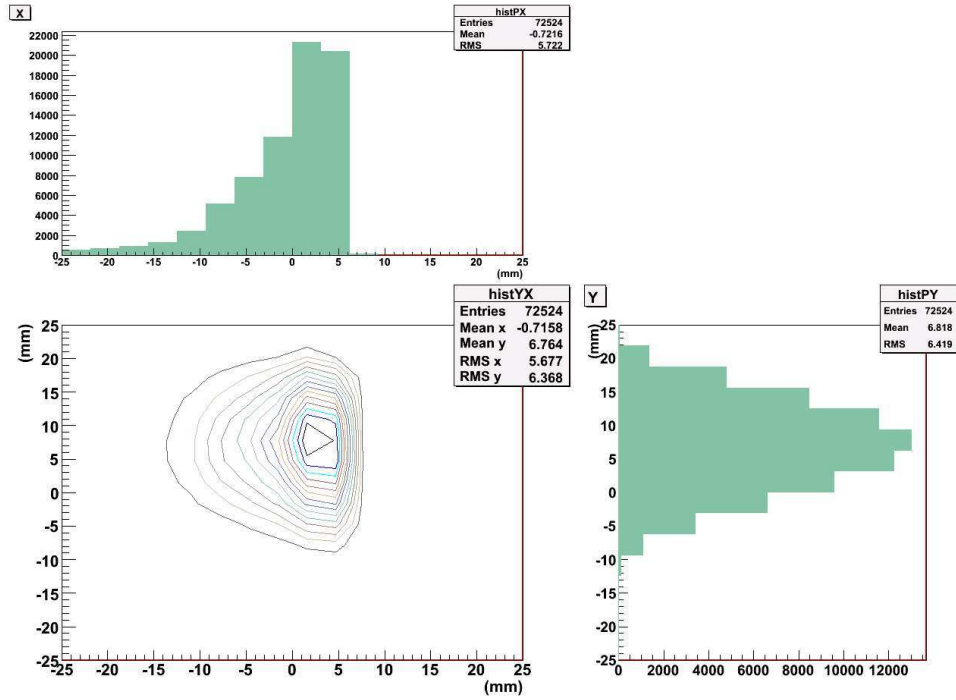


Figure 4.1: No collimator, charge slits, source centered

an energy distribution similar to Figure 4.2, this results in a significant amount of lower energy α particles, these particles bend with a smaller radius in the magnetic dipole (see Equation 2.7) and give rise to the tail seen in all of the charge slit hit patterns.

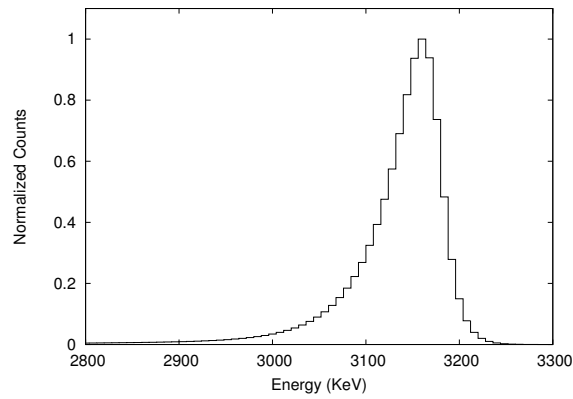


Figure 4.2: Energy distribution of the ^{148}Gd α source.

The offset in the y direction is more difficult to explain and unlike the low energy tail,

is not expected. Since DRAGON is symmetric in the y direction¹ there must be an aspect of DRAGON that is non-ideal. Simulations show that a shift in the source position in the gas target of 2mm down, will cause a shift in the y distribution at the charge slits of ≈ 6 mm. This simulation is shown in Figure 4.3 along with a simulation where the source is not moved. This is discussed more in the next section of this report, Section 4.2. The position of the detector was checked to make sure it was on the beam axis of DRAGON, it agreed within 1mm.

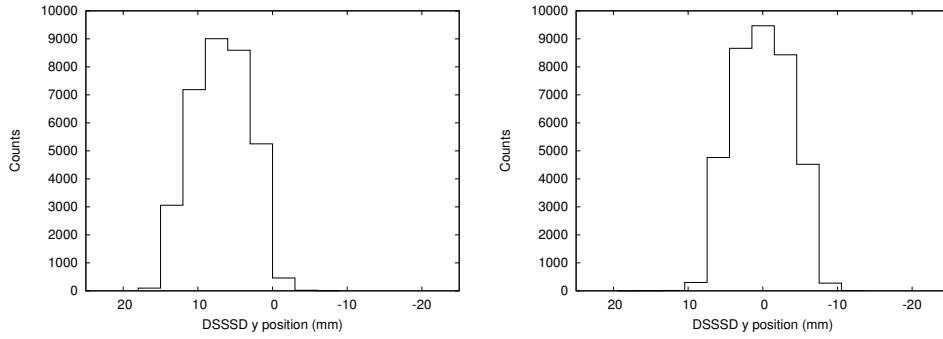


Figure 4.3: GEANT simulation of y distribution at the charge slits with the source moved down 2mm (left) and centered (right). Simulation results are binned in 3mm bins to simulate the DSSSD detector.

Figures A.1 through A.5 show that the beam at the charge slits is out of focus, due to the positions of the beam spots in each image, the focal point is located upstream of the charge slits. This problem will be discussed more in Section 4.2.1.

The transmission percentages allow a look into where particles are being lost. This report assumes that all particles reach the charge slit detectors, therefore the transmission at the charge slits is 100%, at further detector locations (mass slits and final slits) the transmission is expected to be lower than 100%. To obtain the transmission percentages the ratio of the hit rates is used. The hit rates at the charge slits are given in Table 4.1 along with the associated statistical uncertainties. They are determined by counting

¹ Several sextupole's theoretically make DRAGON not symmetric in the y direction, however, before the charge slits there is only one sextupole, its effect is thought to be negligible.

all observed hits between 2700 keV and 3400 keV and dividing by the time of the run. Detector efficiency is ignored and does not effect the transmission.

Collimator	Rate ($\frac{\text{counts}}{\text{second}}$)
Left	2.37 ± 0.02
Right	2.66 ± 0.04
Up	2.83 ± 0.01
Down	2.43 ± 0.03
Out	23.04 ± 0.09
Hole	2.49 ± 0.03

Table 4.1: Hit rates observed at the charge slits. Directions are looking upstream at the collimator.

4.1.2 Mass Slits

Figures A.6 through A.10 show the observed hit patterns at the mass slits, along with the x and y projections for all five collimator positions, these images appear in Appendix A. Positive x -values on the DSSSD chip are closest to the outer edge of DRAGON. Positive y -values are above the beam axis. The measurement where no collimator was used, is shown in Figure 4.4.

Similar to the charge slit measurements all the mass slit measurements share a common features, there is a tail extending into the negative y direction. This is reproduced in simulations when the y distribution at the charge slits is shifted upwards which is the behavior observed at the charge slits. Therefore, the simulated y distribution at the mass slits, if the source is positioned 2mm down in the target box, accurately reproduced the observed data, this is shown in Figure 4.5 along with the distribution when the source is not moved, this provides further evidence for source and/or gas target mis-alignment.

The hit rates and transmission percentages are presented in Table 4.2. The transmission represent the total percentage of particles that were transmitted from the charge slits to the mass slits.

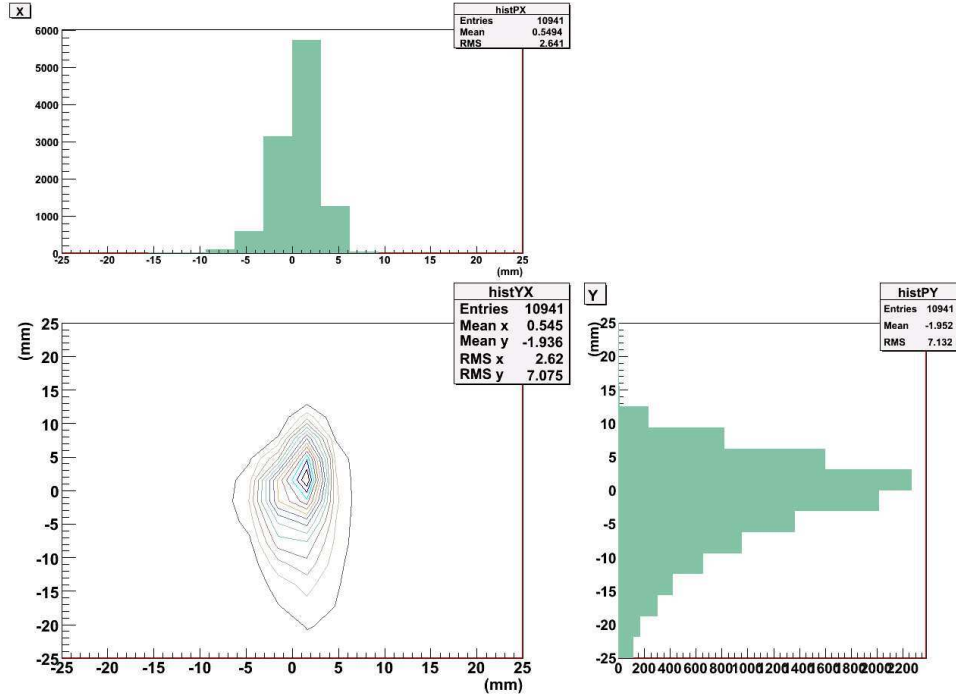


Figure 4.4: No collimator, mass slits, source centered

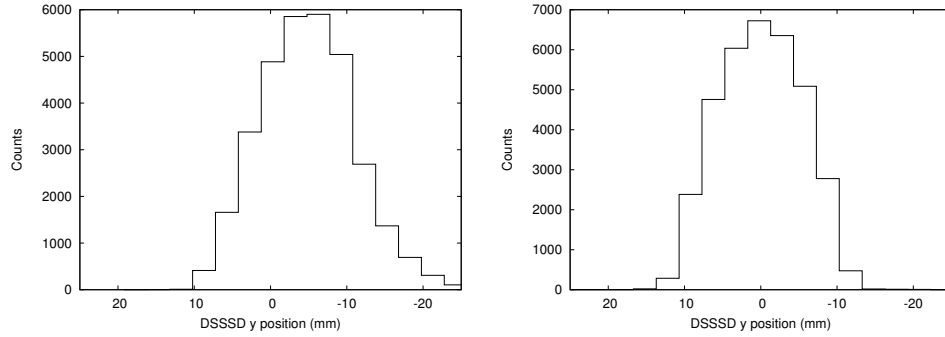


Figure 4.5: GEANT simulation of y distribution at the mass slits with the source moved down 2mm (left) and centered (right). Simulation results are binned in 3mm bins to simulate the DSSSD detector. The tail extending to negative y values is clear in the image on the left.

Of particular interest in this table is the bold value of 80.8% transmission when no collimator is present, this represents DRAGON's transmission at the mass slits for nominal settings.

Collimator	Rates ($\frac{\text{counts}}{\text{second}}$)	Transmission (%)
Left	2.04 ± 0.03	86.3 ± 1.5
Right	1.65 ± 0.02^a	62.1 ± 1.2
Up	2.63 ± 0.04	93.1 ± 1.5
Down ^b	1.60 ± 0.02	66.0 ± 1.2
Out	18.61 ± 0.18^c	80.8 ± 0.8
Hole	2.31 ± 0.01	92.9 ± 1.2

^a large particle losses (10-15%) due to finite detector size, see Figure A.7

^b This result is questionable due to increased rate observed in Table 4.3, see Section ?? for discussion.

^c Small particle loss due to finite detector size

Table 4.2: Hit rates and transmissions observed at the mass slits. Directions are looking upstream at the collimator.

4.1.3 Final Slits

Figures A.11 through A.15 show the observed hit patterns at the final slits, along with the x and y projections for all five collimator positions, these images appear in Appendix A. Positive x -values on the DSSSD chip are closest to the outer edge of DRAGON. Positive y -values are above the beam axis. The measurement where no collimator was used, is shown in Figure 4.6.

Unlike the charge and mass slits, simulations are unable to accurately reproduce the hit pattern observed in Figure 4.6. Of particular interest in this figure is the y correlation with x position, on inspection of Figure A.11 and A.12 we see that particles initially entering the left collimator end up with a higher y value and particles entering the right collimator have a lower y value.

The shift in the source position does not have a large effect on the simulated results, one aspect of both simulations is that the large x tail is not within the detector region. Comparing this with the experimental results we see that there is a horizontal shift between the hit patterns.

When simulating transmissions at the charge slits, we do not include particles that are

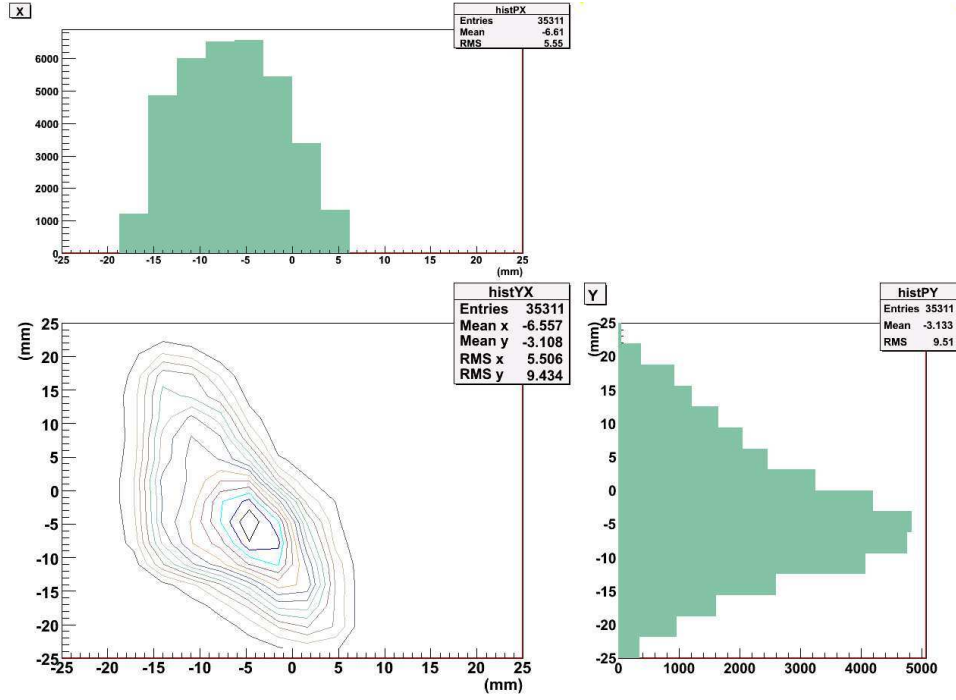


Figure 4.6: No collimator, final slits, source centered

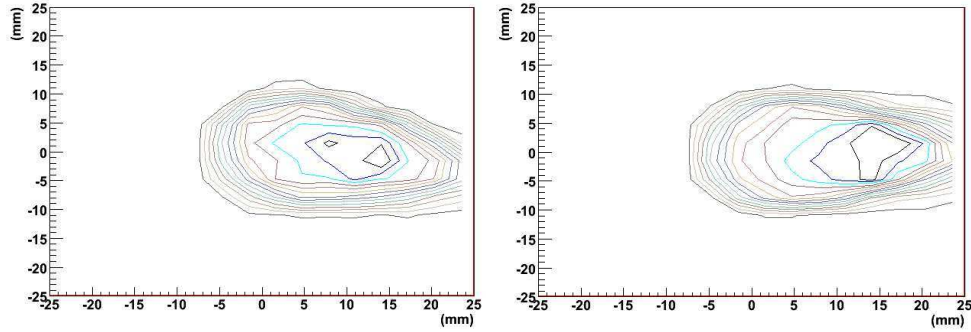


Figure 4.7: GEANT simulation of hit pattern at the final slits with the source moved down 2mm (left) and centered (right). Simulation results are binned in 3mm bins and then contoured to simulate the DSSSD detector.

not in the DSSSD region, even though they may continue on in the separator and make it to the mass or final slit DSSSD region. The justification for this is because the observed hit pattern will theoretically suffer from this effect as seen in Figures A.2 and 4.1. When simulating transmissions at the final slits however, we include particles that are not in the DSSSD region but still make it to the final slits. This is justified mainly because

the experimental hit patterns clearly do not suffer from this same effect (loss at high x positions). When no collimator is used, this results in a $\approx 1\%$ transmission difference. Of all the collimators, only the right orientation collimator is affected, here the transmission difference is $\approx 6\%$. These numbers (simulated transmissions), along with observed hit rates and transmission between the charge slits and final slits are presented in Table 4.3.

Collimator	Rates ($\frac{\text{counts}}{\text{second}}$)	Transmission (%)	Simulated Transmission (%)
Left	1.25 ± 0.02	52.8 ± 1.0	94.5 ± 0.8 (93.5 ± 0.8)
Right	1.05 ± 0.02^a	39.7 ± 0.7	79.4 ± 0.7 (53.4 ± 0.5)
Up	2.73 ± 0.01	96.7 ± 0.5	99.2 ± 0.8 (84.8 ± 0.7)
Down	2.18 ± 0.02	89.7 ± 1.4	99.2 ± 0.8 (97.3 ± 0.9)
Out	16.16 ± 0.09	70.2 ± 0.5	95.0 ± 0.7 (83.4 ± 0.7)
Hole	2.36 ± 0.02	94.6 ± 1.4	99.3 ± 0.7 (95.1 ± 0.7)

^a medium particle losses (10-15%) due to finite detector size, see Figure A.12

Table 4.3: Hit rates and transmissions observed/simulated at the final slits. Directions are looking upstream at the collimator. Simulated transmissions are for nominal settings, the numbers in the brackets indicate transmissions when the source is moved down 2mm in the gas target box.

These observed transmissions highlight that particles emitted left and right are being lost the most in DRAGON while particles emitted up and down are transmitted well. Simulation transmissions for DRAGON's nominal settings show slight particle loss for left and right emitted particles with almost full transmission for particles emitted up and down. When the source position is moved down in the GEANT simulation there is a more dramatic effect on the transmission, overall the simulated transmission drops by $\approx 12\%$

Figure 4.8 shows the locations of particle losses in DRAGON for the nominal tune with no collimator. Each set of losses is labeled by the element in DRAGON that stopped the particles.

The majority of particle loss occurs inside quadrupoles at locations where the beam envelope is large, this can be seen by matching particle losses to corresponding locations in Figure 3.2. From this diagram three different types of particle loss can be seen. All the

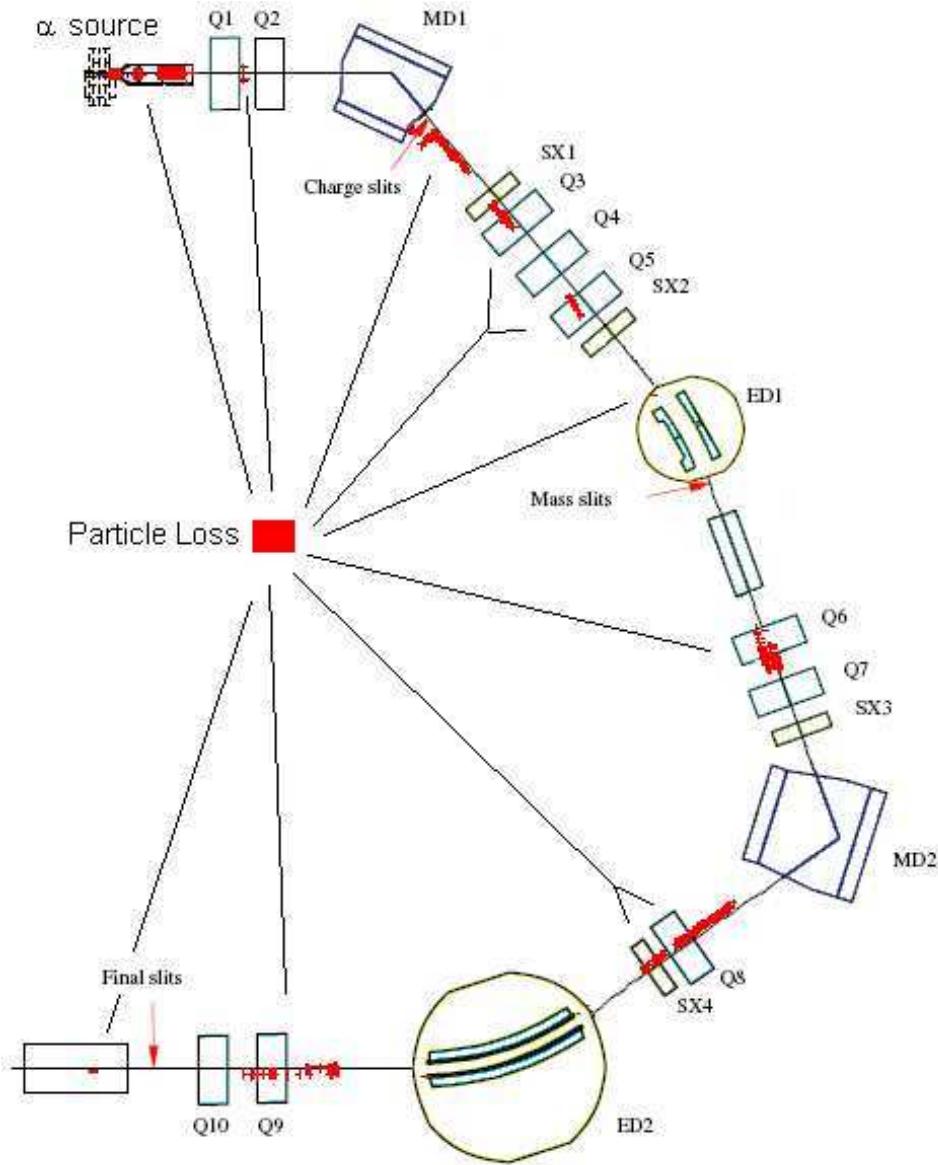


Figure 4.8: Stopping distances in DRAGON along with corresponding elements in DRAGON. Distance is measured along axis of DRAGON.

particle loss in the gas target corresponds to particles that did not meet the geometric acceptance criteria of DRAGON, these are ignored when calculating transmission because they never enter the separator to begin with. The second type of particle loss is particles with low energy, these particles get removed at or immediately after the charge slits. The final particle loss is, as mentioned above, in quadrupoles where the beam envelope is large.

With the exception of some particle loss on both sides of the Q6-Q7 doublet, all particle loss originates from particles emitted to the right, looking upstream.

4.1.4 Conclusions

The asymmetry in the hit rates (see Table 4.1) was investigated further by removing the first pumping tube downstream of the gas target (see Figure 2.3). The observed asymmetry in the hit rates was much smaller after this pumping tube was removed suggesting particles in the initial 22 mrad cone were being lost on this piece of equipment.

Both the charge slits and the mass slits suggest that there is a misalignment in the y direction. This alignment is most easily checked by moving the source position in the gas target. In simulations, moving the source 2mm below the beam axis accurately reproduces the observed behavior at the charge and mass slits. Other misalignments in DRAGON also cause the observed behavior, moving the first quadrupole up by 1mm for example, but target misalignment is also suggested by the observed rates at the charge slits before and after an element of the pumping tube system was removed. Before the pumping tube was removed, the rate for the down collimator was 2.43 counts/second, after the collimator was removed the count increased to 2.73 counts/second. The up and right orientations of the collimator were not affected by the removal. The left showed a similar effect as the down collimator where the rate increases from 2.37 counts/second to 2.74 counts/second.

DRAGON is very sensitive to changes in the vertical position of the source but not as sensitive to horizontal changes. Due to this this reason we assume any deviations in the horizontal direction do not affect the transmission drastically and can be ignored for now. For a more quantitative description on this see Table 4.4. This table gives the first-order transfer matrix elements of DRAGON at each of the three detector locations, $(\alpha|\beta)$

denotes the affect on the α component at the detector location due to initial deviations in the β component at the source.

Finally, the mass slit transmission rates are in disagreement with the final transmission rates, the up, down and hole collimators result in increased transmission rates. It is possible that larger than usual noise problems at the mass slits could result in decreased rates although this issue was thoroughly examined.

Matrix Element	Charge Slits	Mass Slits	Final Slits
$(x x)$	-0.440	0.689	0.980
$(y y)$	-3.554	0.980	-1.767

Table 4.4: First-order transfer matrix elements in DRAGON, x is horizontal position and y is vertical position

To test the hypothesis that the gas target box is below the beam axis of DRAGON, the source is moved up by 2mm in the gas target box. If this is the case we should see the artifacts in Figures 4.3 (off axis in y) and 4.3 (extended tail into $-y$) disappear. These results are presented in the next section.

4.2 Source Displaced 2mm up in Target Box

4.2.1 Charge Slits

Figures B.1 through B.5 show the observed hit patterns at the charge slits after the source was moved up 2mm, along with the x and y projections for all five collimator positions, these images appear in Appendix B. Positive x -values on the DSSSD chip are closest to the outer edge of DRAGON. Positive y -values are above the beam axis. The measurement where no collimator was used, is shown in Figure 4.9.

As predicted, the vertical shift observed in the previous section disappeared when the source was moved up 2mm, although, Figures B.1 through B.5 are still de-focused at the charge slits. This problem can be compensated for by lowering the intensity of the first

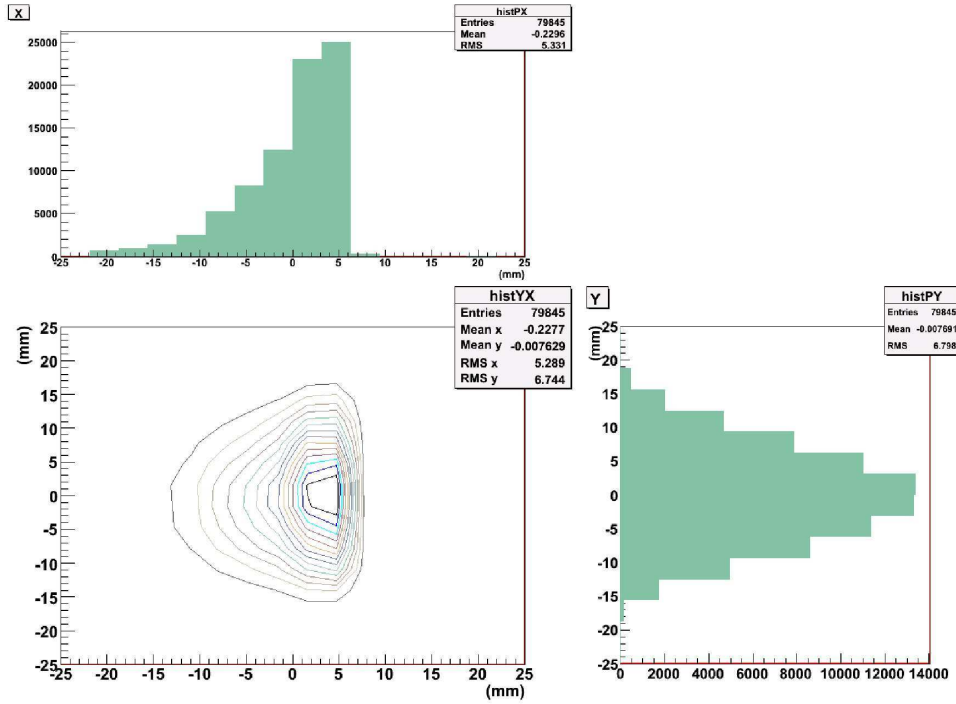


Figure 4.9: No collimator, charge slits, source moved up 2mm

quadrupole by $\approx 5\%$. The resulting, no collimator, hit pattern is shown in Figure 4.10. This hit pattern is much more condensed and although no additional collimator data was taken, the size of the hit pattern suggests that the beam is in focus. Reference [6], a previous acceptance study, sees this behaviour as well by observing hit pattern widths.

Hit rates for the charge slits measurements with the source moved up 2 mm are shown in Table 4.5. As mentioned above, these hit rates are more symmetric after the removal of one of the pumping tubes.

4.2.2 Mass Slits

These experiments were not performed due to time constraints but should be checked for agreement with simulation. Since the y -axis shift at the charge slits is gone, presumably the extended $-y$ tail is also gone.

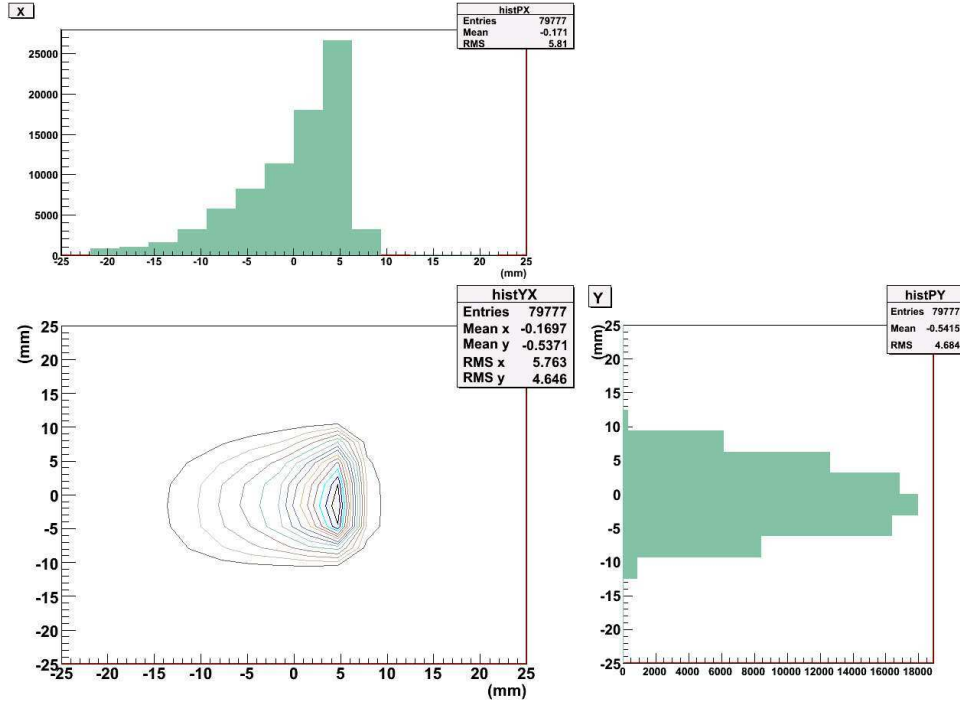


Figure 4.10: Hole collimator, charge slits, source moved up 2mm and quadrupole 1 at -5% of its nominal value.

Collimator	Rate ($\frac{\text{counts}}{\text{second}}$)
Left	2.754 ± 0.006
Right	2.66 ± 0.03
Up	2.732 ± 0.007
Down	2.81 ± 0.03
Out	25.08 ± 0.09
Hole	2.52 ± 0.02

Table 4.5: Hit rates observed at the charge slits with the closest pumping tube removed and the source moved up. Directions are looking upstream at the collimator.

4.2.3 Final Slits

The final set of measurements were performed at the final slits. Figures B.6 to B.10 show the observed hit patterns at the final slits after the source was moved up 2mm, along with the x and y projections for all five collimator positions, these images appear in Appendix B. Positive x -values on the DSSSD chip are closest to the outer edge of DRAGON. Positive y -values are above the beam axis. The measurement where no collimator was

used, is shown in Figure 4.11.

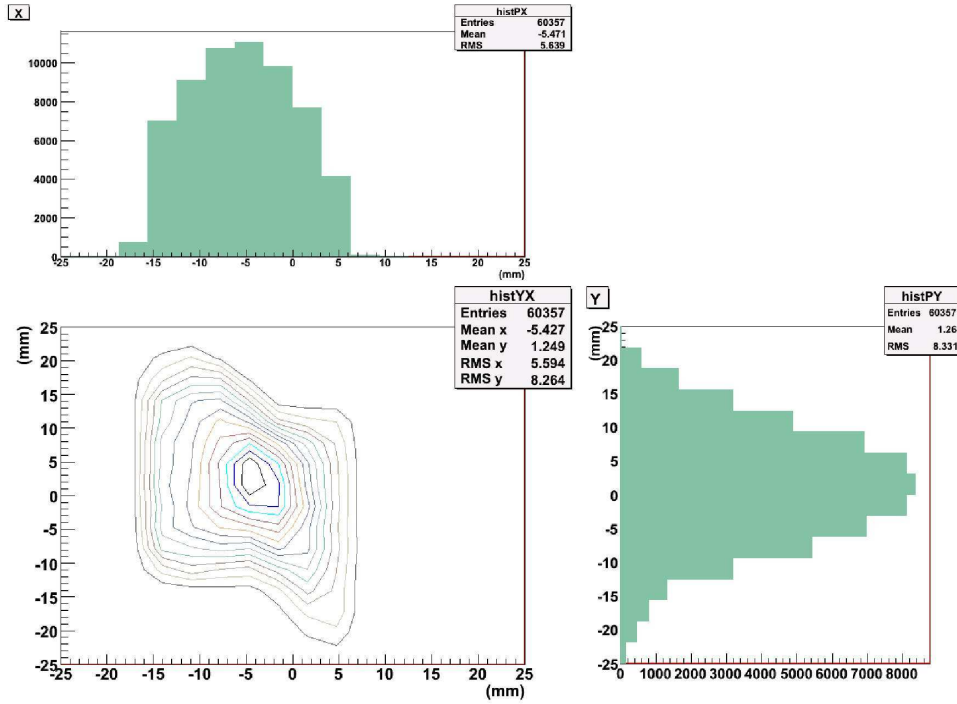


Figure 4.11: No collimator, final slits, source moved up 2mm

Simulations did not predict the observed hit pattern at the final slit even after the source was simulated to be lower than the beam axis. Since these simulated hit patterns fail to agree with experiment, the effect of moving the source is unknown. After measurement, it can be seen that the main difference is that the max of the y distribution has moved to zero, up from ≈ -5 mm. The shift in the hit patterns obtained through the left and right collimators is still present suggesting another misalignment is having an effect on the beam. Possible suggestions are eluded to in the next Section (Conclusions and Future Work on Acceptance).

Transmission percentages and hit rates were observed at the final slits and are presented in Table 4.6. Included for reference is the transmissions at the final slits with the source in the original position. No simulated data is included because both versions were presented in Section 4.1.3.

Collimator	Rates ($\frac{\text{counts}}{\text{second}}$)	Transmission (%)	Transmission (old position) (%)
Left	1.146 ± 0.004	42.0 ± 1.0	52.8 ± 1.0
Right	1.58 ± 0.013	59.4 ± 0.8	39.7 ± 0.7
Up	2.53 ± 0.014	92.6 ± 0.6	96.7 ± 0.5
Down	2.49 ± 0.018	88.6 ± 1.1	89.7 ± 1.4
Out	17.16 ± 0.07	68.4 ± 0.4	70.2 ± 0.5
Hole	2.464 ± 0.009	97.8 ± 0.9	94.6 ± 1.4

Table 4.6: Hit rates and transmissions observed at the final slits with source moved up. Directions are looking upstream at the collimator.

There are several interesting values that arise in this data set. The left transmission went down (about 20%), for a possible solution to this refer to Section 5, point 5. The right transmission increased by $\approx 50\%$, this increase agrees with the simulated transmission increase.

CHAPTER 5: CONCLUSIONS AND FUTURE WORK ON ACCEPTANCE

The goal of these acceptance studies is not to make DRAGON perfect for all reactions at all cone angles or to obtain the maximum transmission¹, rather what is needed is for DRAGON to agree with simulations so that accurate efficiency fractions can be determined through simulations for previous and upcoming reactions. These efficiency fractions are used directly to determine the yield (Equation 2.4) which is one of the properties DRAGON was designed to measure. Another goal of these acceptance studies is to pinpoint possible problems in DRAGON such as misalignments or tuning problems and correct them.

This study has determined the following conclusions and suggestions for implementation.

1. DRAGON's gas target needs to be re-aligned to insure that the gas target's axis is on axis with the beam coming from ISAC as well as, and possibly more important, the spectrometer axis. This ensures that the best part of the incoming beam interacts with the gas but also ensures that the EMS will receive particles on axis.

2. If possible a system wide survey of the present location of every element in DRAGON would be useful for future referencing if misalignment issue arise. A survey with a theodolite concluded that the gas target was high with respect to the beam axis. This is in addition to a report which concludes the gas target is lower then the beam line, [4].

¹ Transmission can be increased in many ways including mistuning of the overall energy setting of DRAGON or by optimizing the ED settings.

3. The first three elements in DRAGON need to be studied in more detail and corrected in order to achieve focus at the mass slits. For excellent beam suppression the slits need to be closed as much as possible without clipping any recoils, this can only be done if the recoils are actually at a focus at the slit locations.

4. Further simulations and experiments must be carried out to pinpoint the cause of the asymmetry in the final hit pattern. There are a lot of elements between the mass slits and the final slits so this may require additional detector locations or some alternative means of observing the hit patterns. Due to the nature of the asymmetry, a possible cause of this and a suggestion for simulations would be to test the effect on the hit pattern due to a rotated quadrupole.

5. Although not included as results in this report, it was found that small changes in the ED's voltage can change the hit rate observed at the final slits. The current method of tuning DRAGON's first ED calls for the centering of the beam on the mass slits, the tuning of the final ED centers the hit pattern on the final slits. This method does not agree with the theoretical settings for the electric dipoles. As an example of this, the ray tracing diagrams shown in Figure 3.2 is not centered at the final slits but rather shifted to negative values of x . Since the detector is located 66cm after the focus, this would give a hit pattern shifted to high x values (as in Figure 4.7), not centered as the tuning description calls for. Figure 5.1 shows the transmission at the final slits for varying ED2 voltages, the theoretical value, based on 80% of the ED1 voltage (81.5kV, which was chosen to center the beam at the mass slits), is 65.2 kV. There was no collimator used in these measurements.

Results in this report use 63.5 kV as the set point on ED2. It is interesting to point out that in all of these measurements (Figure 5.1) the beam at the final detector position is fully on the chip with empty channels at the edge, this means that any particle losses are occurring in the separator itself. The left collimator was tested at an ED2 setting of 63.0

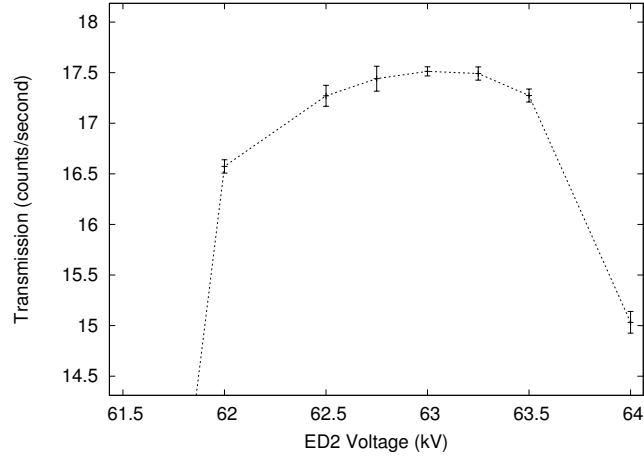


Figure 5.1: Effect on transmission with varying ED2 voltage setting.

kV to see if the transmission increased, the result was a transmission of 1.169 ± 0.004 counts/second. At 62.5 kV the transmission was 1.14 ± 0.012 counts/second. Finally at 64.0 kV, the transmission was 1.15 ± 0.011 counts/second. Since steering the beam both ways in DRAGON does not seem to increase the transmission at the final slits the problem may occur before the second ED. From 4.8 and included in the discussion with it, the Q6-Q7 doublet shows particle loss in simulations for particles emitted to the right as well as left (looking upstream). This is the only quadrupole location in Dragon that particles originally emitted to the left are lost² and should be investigated further.

It is possible to increase the transmission by $\approx 15\%$ by reducing ED1's voltage setting by 2 kV, this may provide clues to particle loss as well.

² With the exception of small Q1-Q2 doublet losses.

APPENDIX A

SOURCE CENTERED IN GAS TARGET IMAGES

A.1 Charge Slit Images

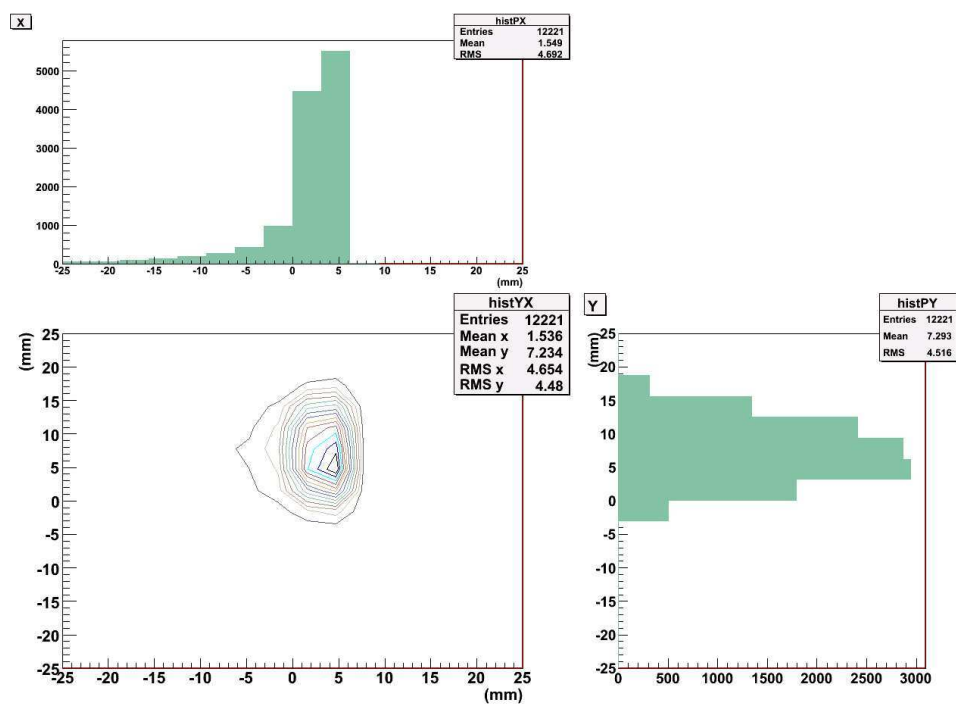


Figure A.1: Collimator in left orientation, charge slits, source centered

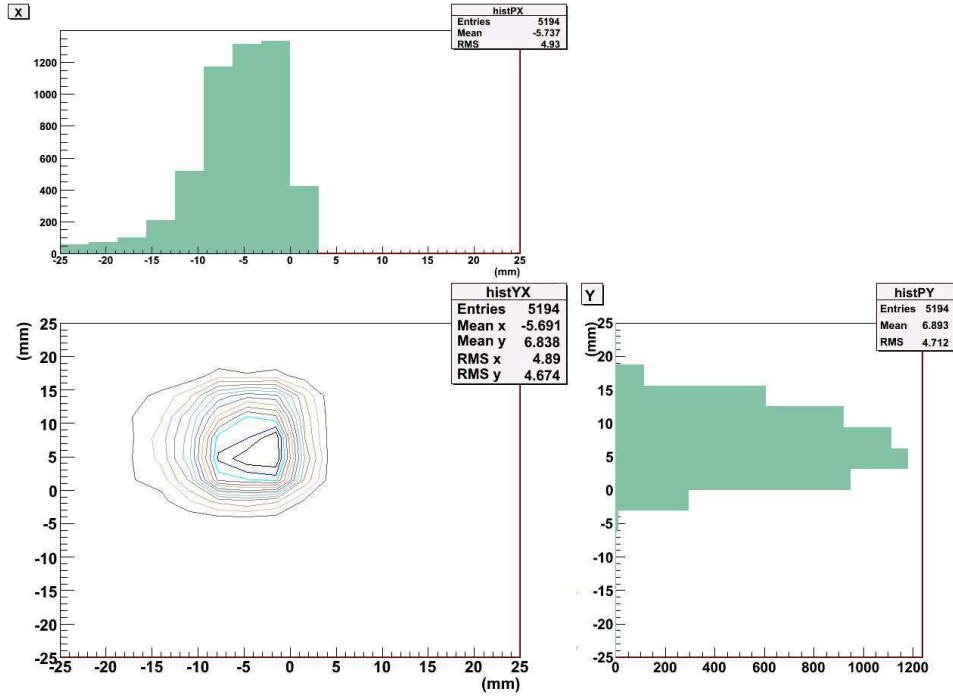


Figure A.2: Collimator in right orientation, charge slits, source centered

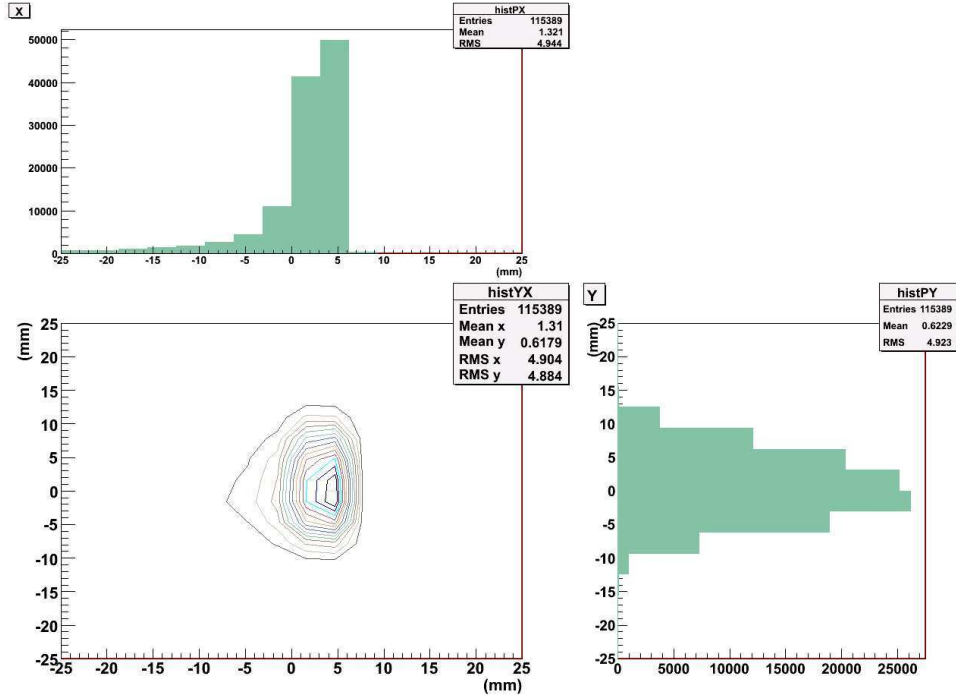


Figure A.3: Collimator in up orientation, charge slits, source centered

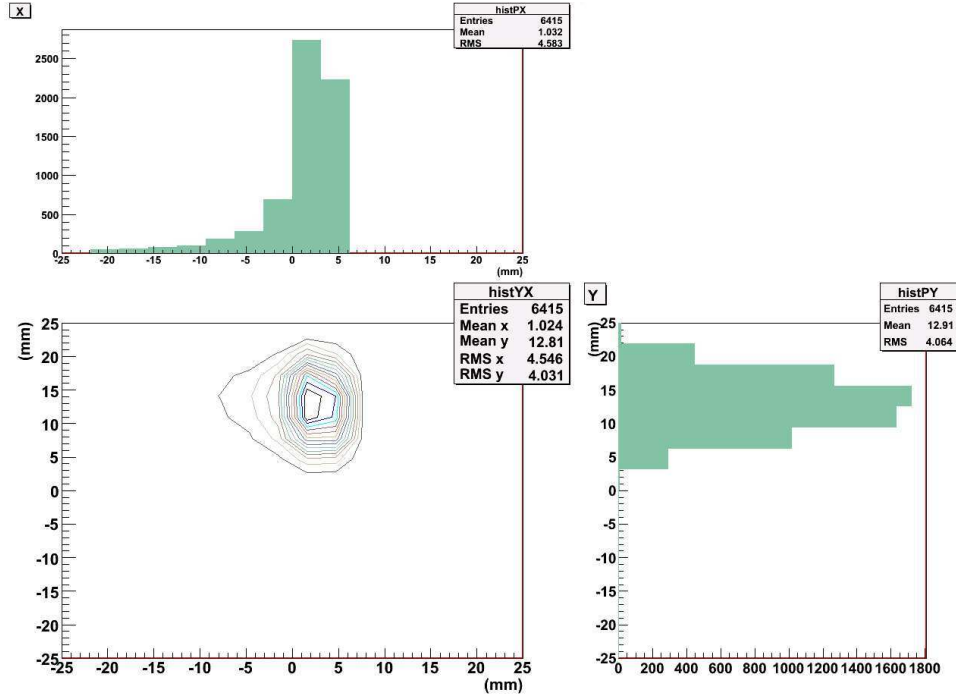


Figure A.4: Collimator in down orientation, charge slits, source centered

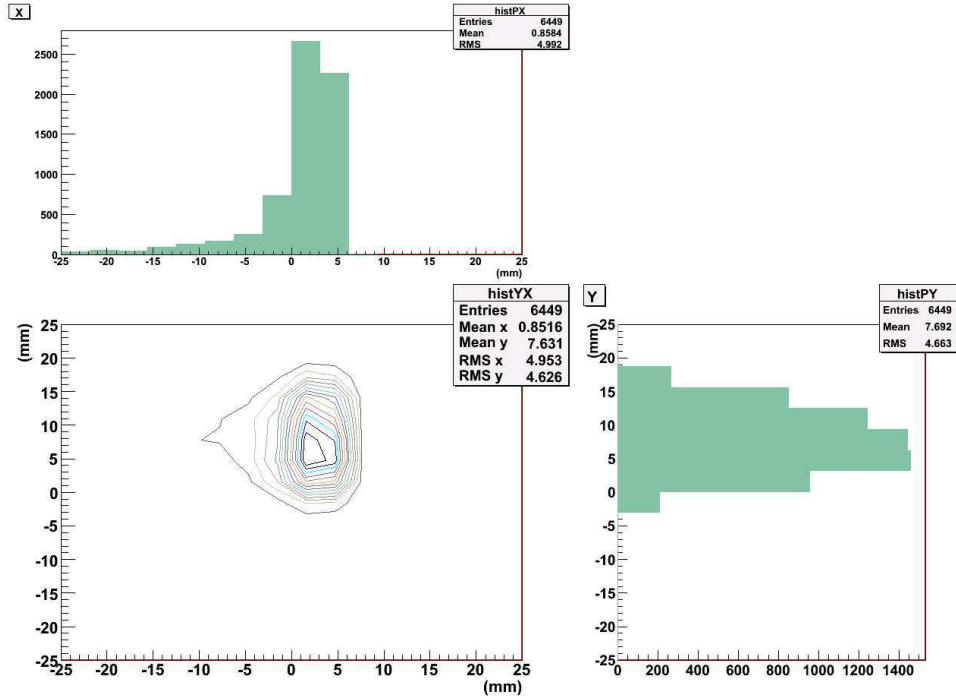


Figure A.5: Collimator in hole orientation, charge slits, source centered

A.2 Mass Slit Images

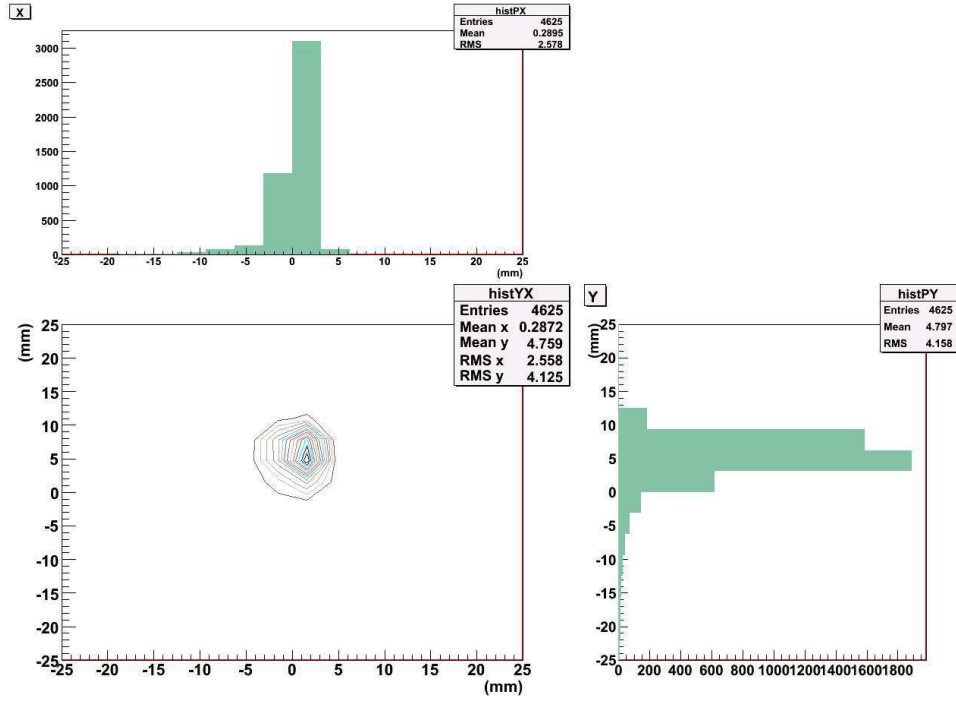


Figure A.6: Collimator in left orientation, mass slits, source centered

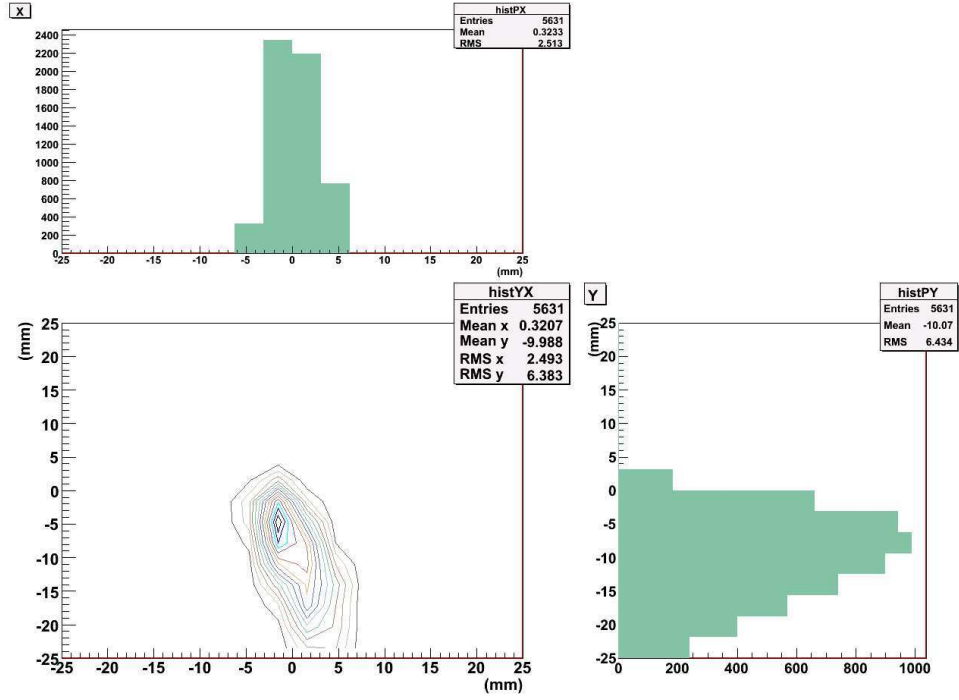


Figure A.7: Collimator in right orientation, mass slits, source centered

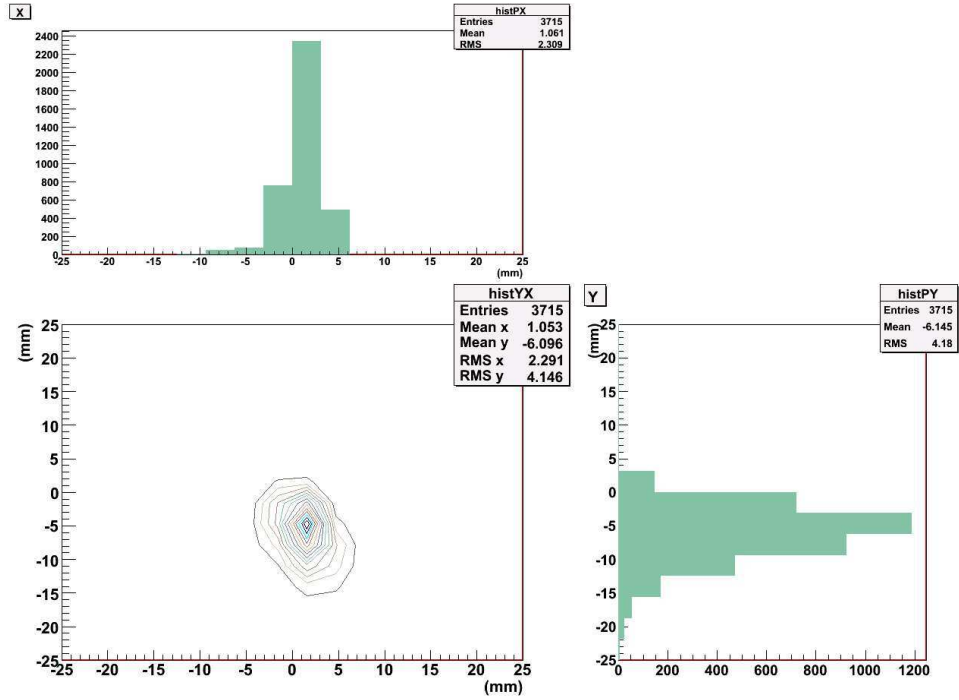


Figure A.8: Collimator in up orientation, mass slits, source centered

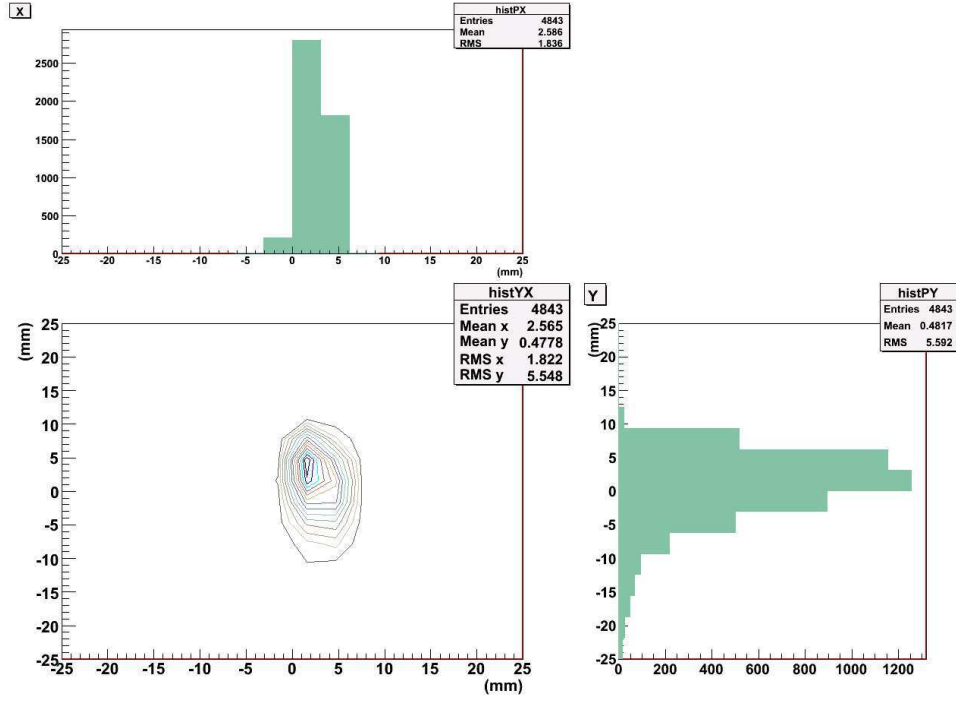


Figure A.9: Collimator in down orientation, mass slits, source centered

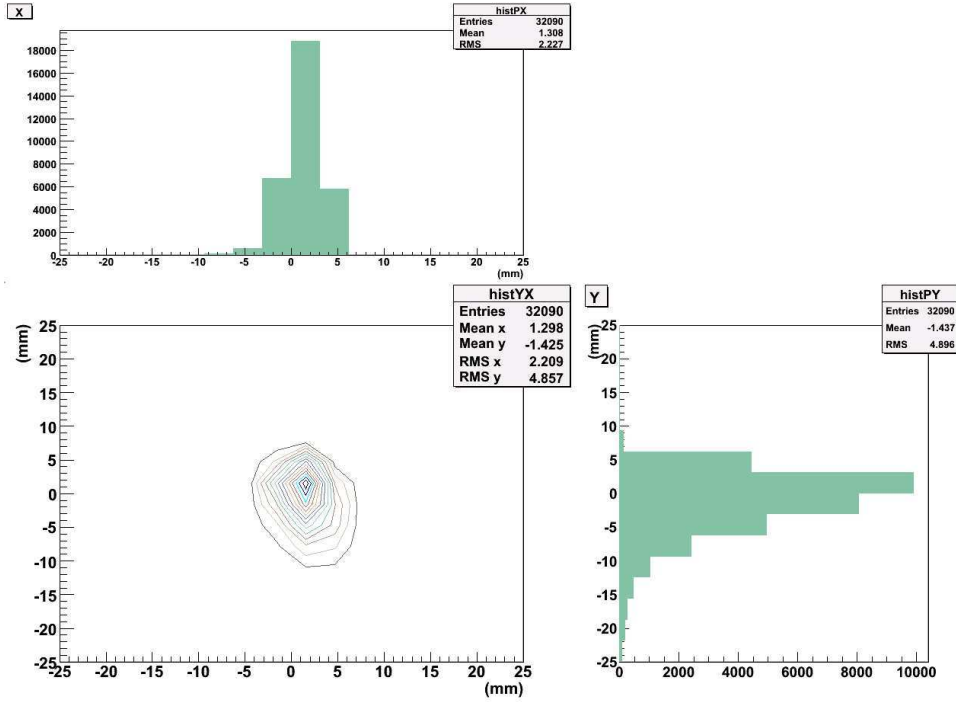


Figure A.10: Collimator in hole orientation, mass slits, source centered

A.3 Final Slit Images

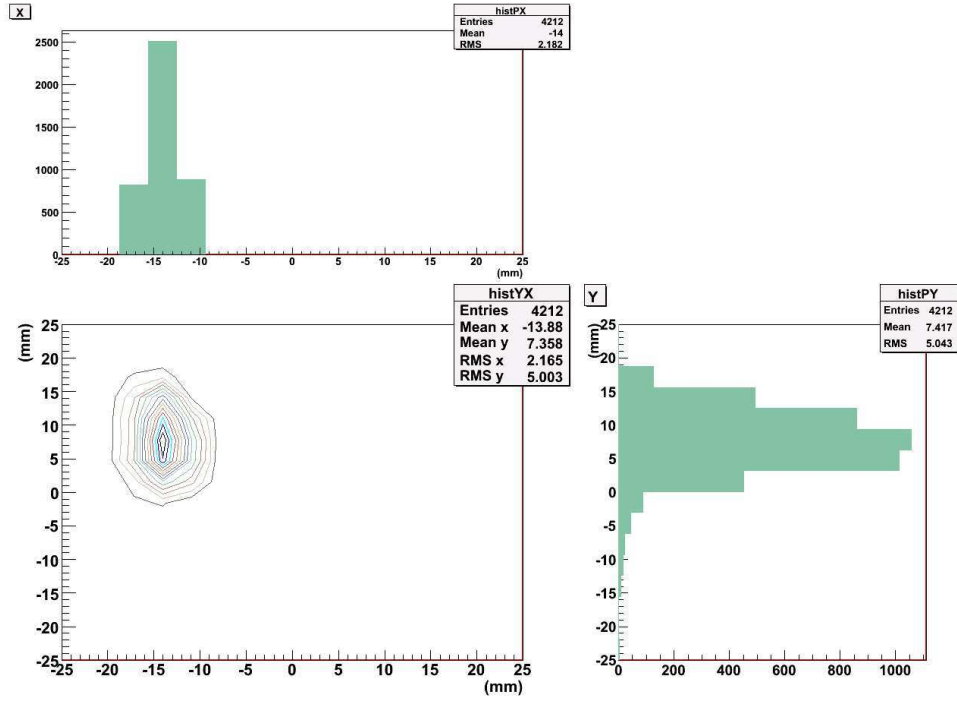


Figure A.11: Collimator in left orientation, final slits, source centered

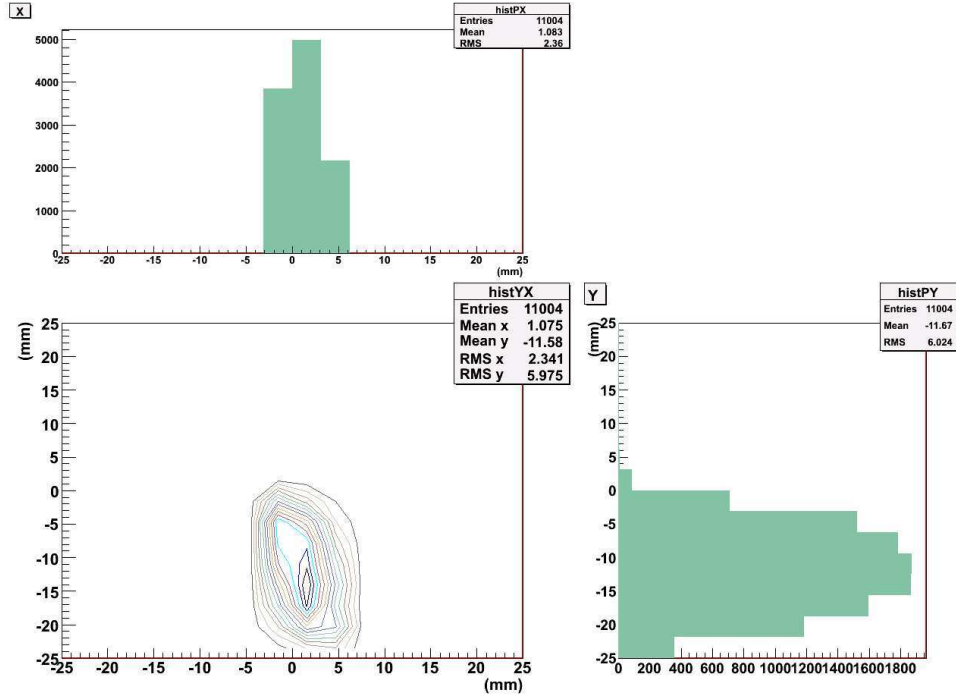


Figure A.12: Collimator in right orientation, final slits, source centered

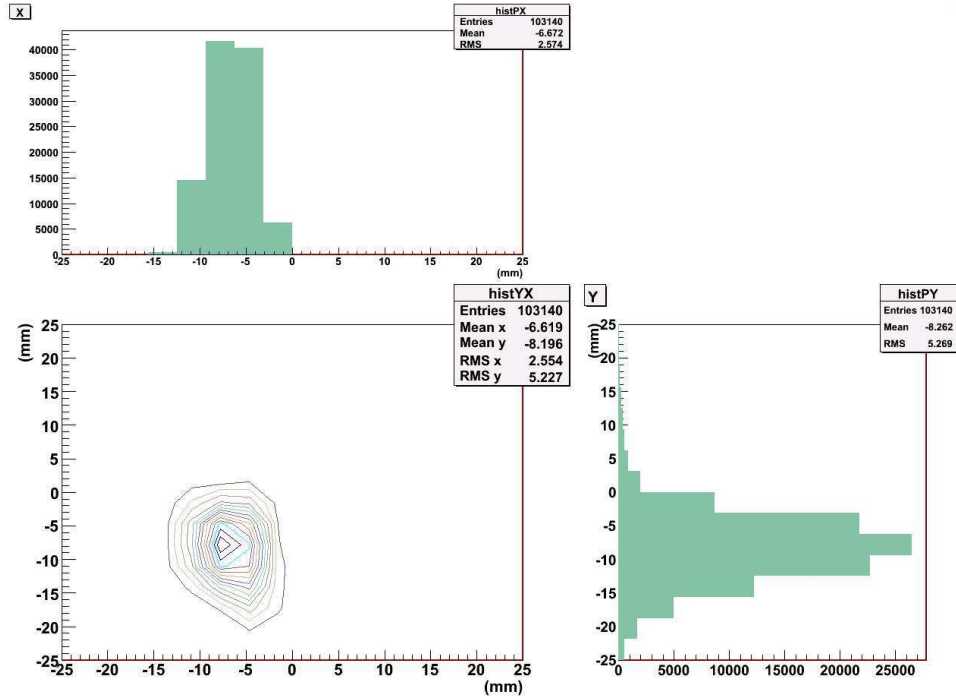


Figure A.13: Collimator in up orientation, final slits, source centered

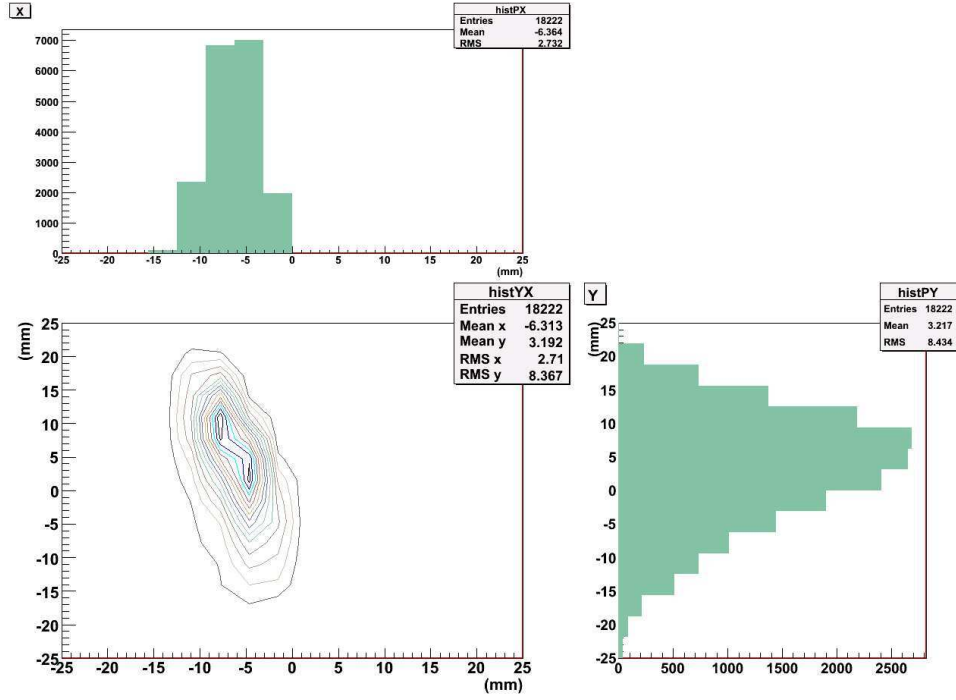


Figure A.14: Collimator in down orientation, final slits, source centered

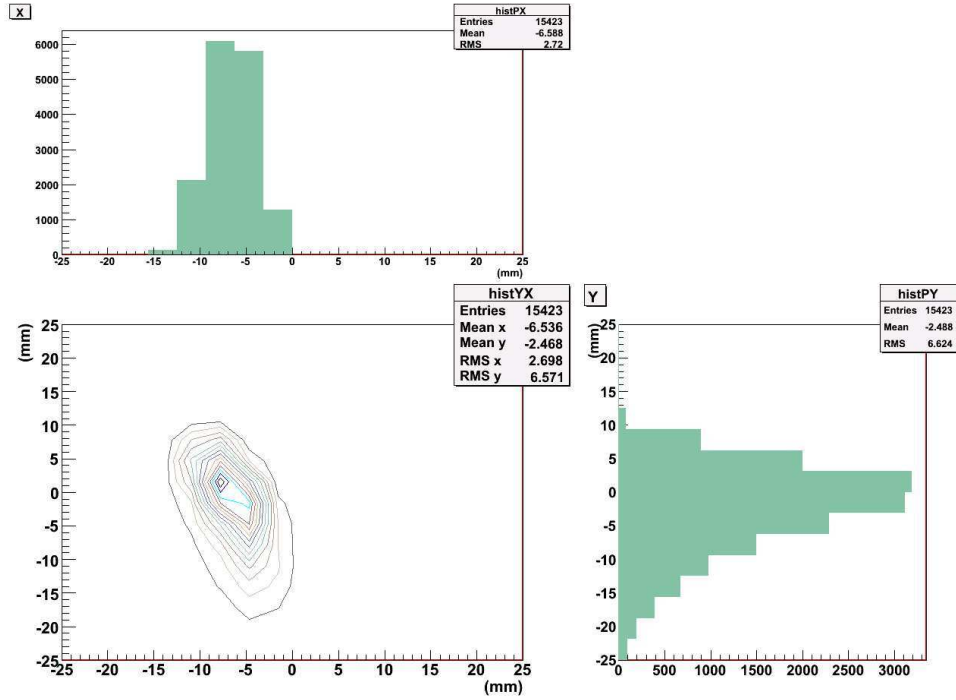


Figure A.15: Collimator in hole orientation, final slits, source centered

APPENDIX B

SOURCE 2MM HIGH IN GAS TARGET IMAGES

B.1 Charge Slits

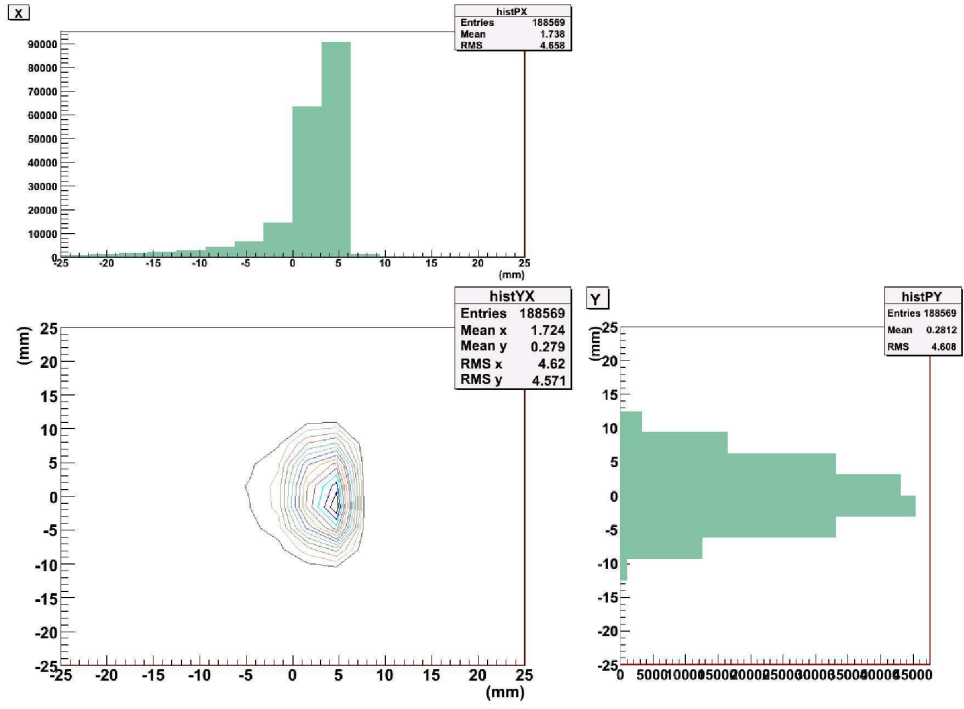


Figure B.1: Collimator in left orientation, charge slits, source moved 2mm up

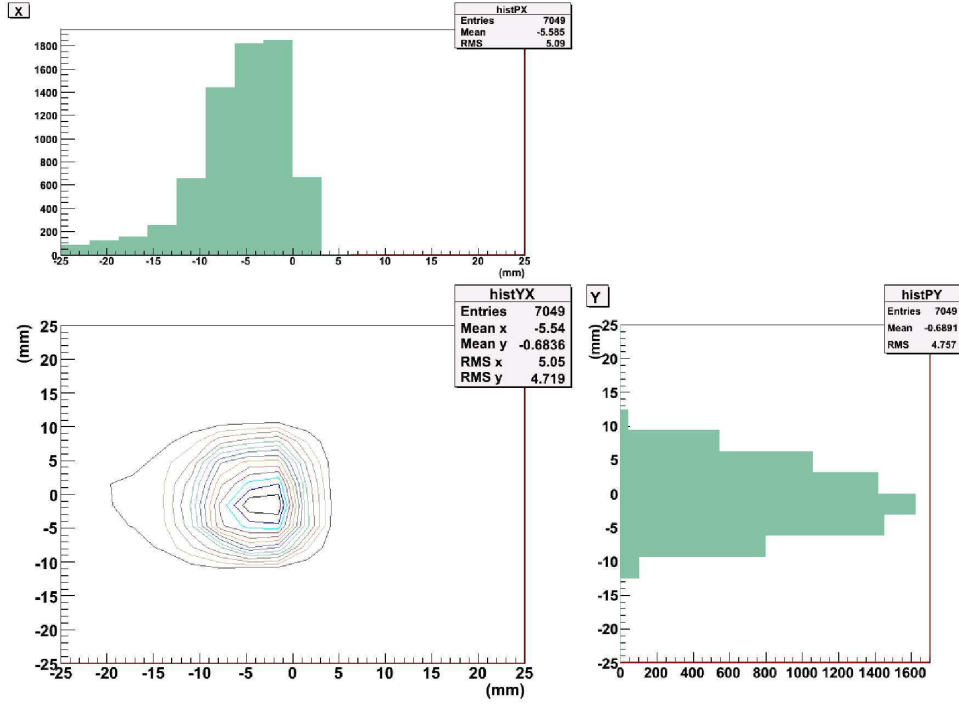


Figure B.2: Collimator in right orientation, charge slits, source moved 2mm up

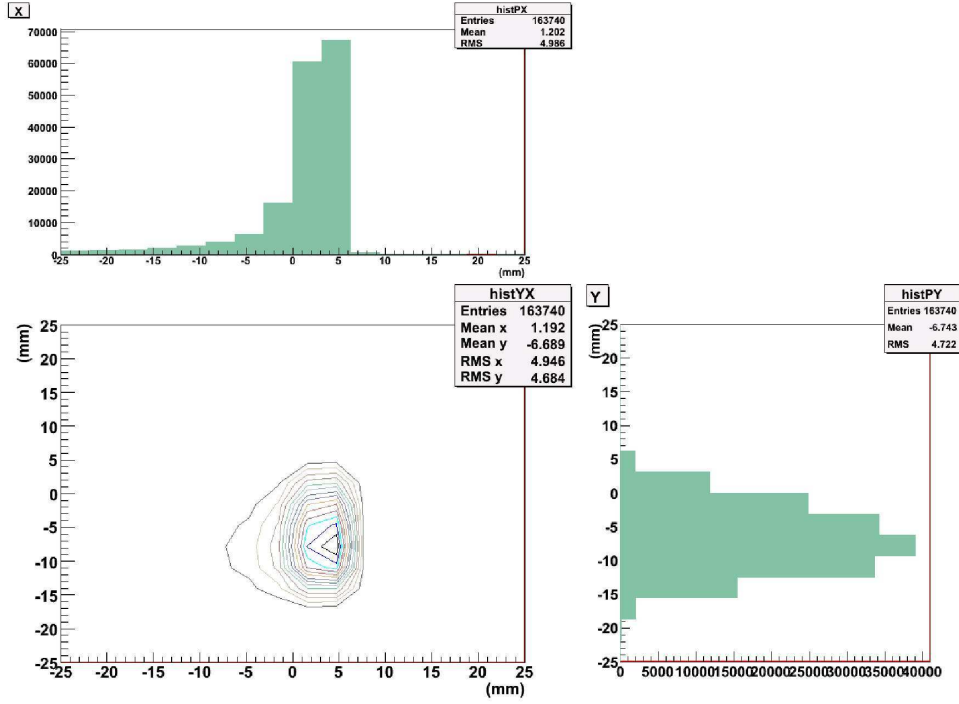


Figure B.3: Collimator in up orientation, charge slits, source moved 2mm up

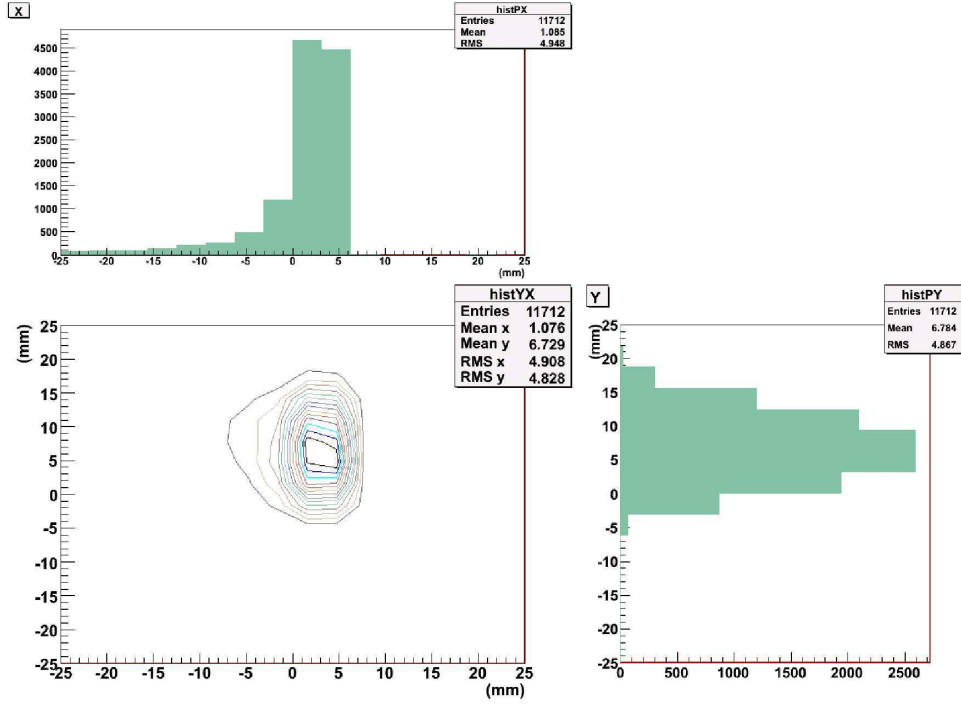


Figure B.4: Collimator in down orientation, charge slits, source moved 2mm up

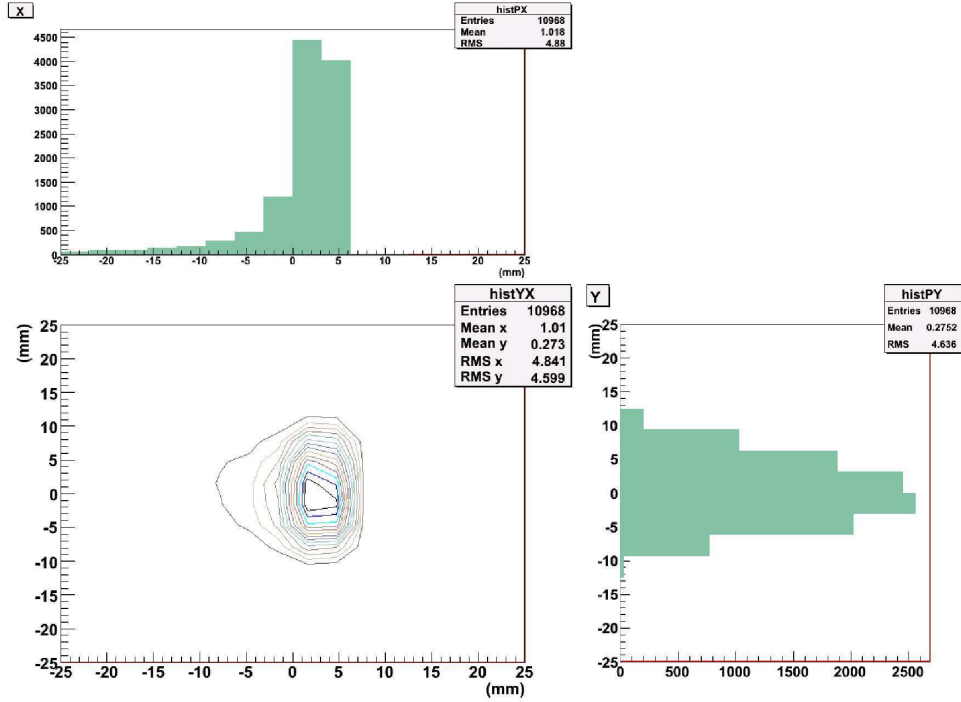


Figure B.5: Collimator in hole orientation, charge slits, source moved 2mm up

B.2 Final Slits

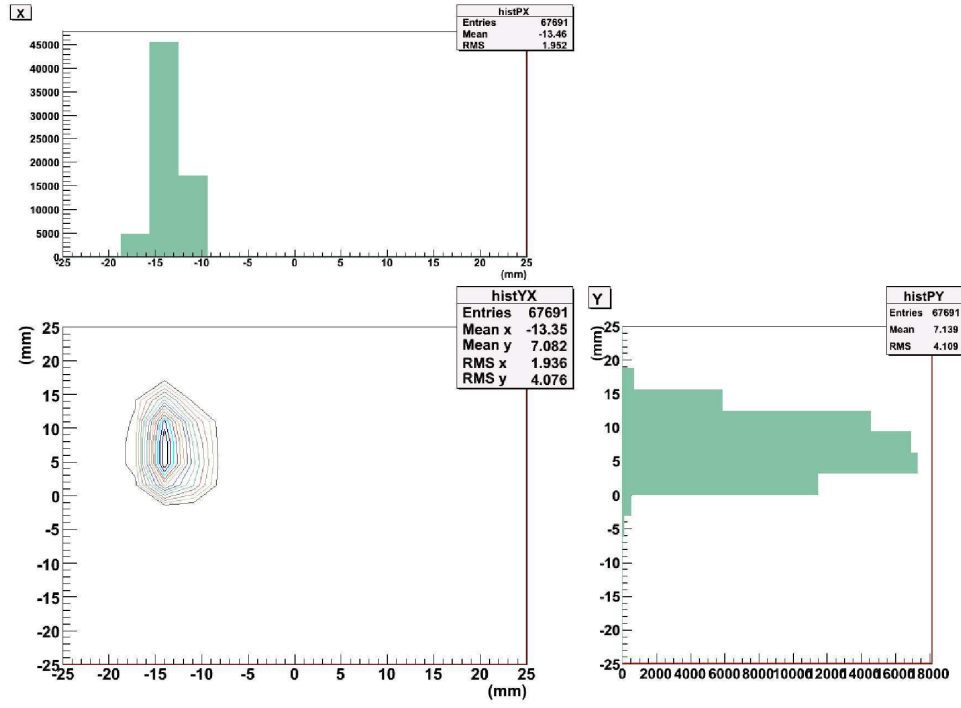


Figure B.6: Collimator in left orientation, final slits, source moved 2mm up

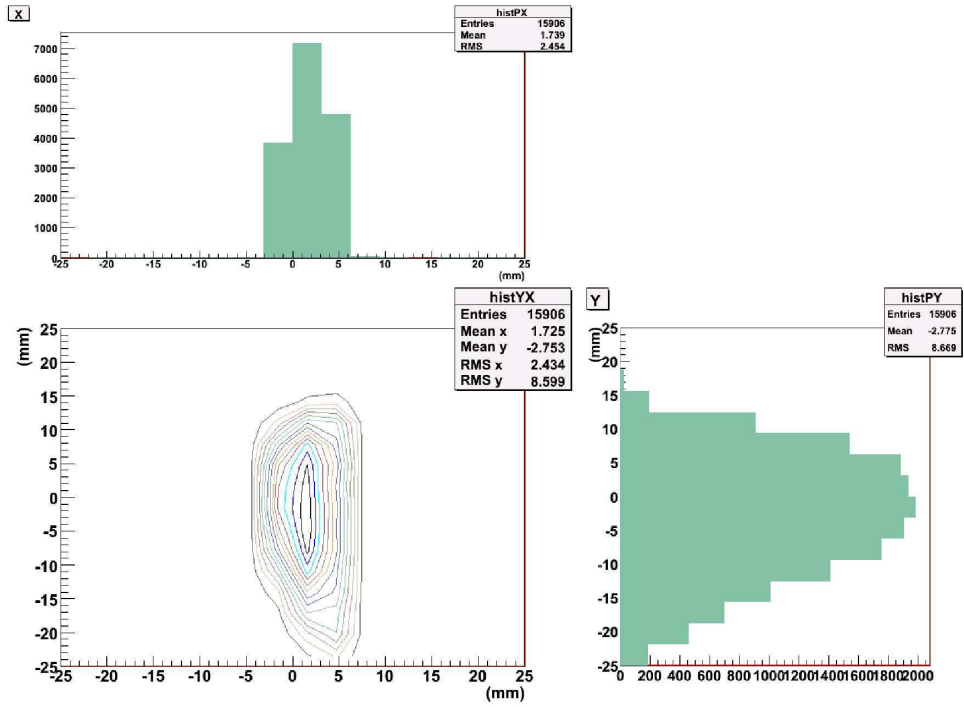


Figure B.7: Collimator in right orientation, final slits, source moved 2mm up

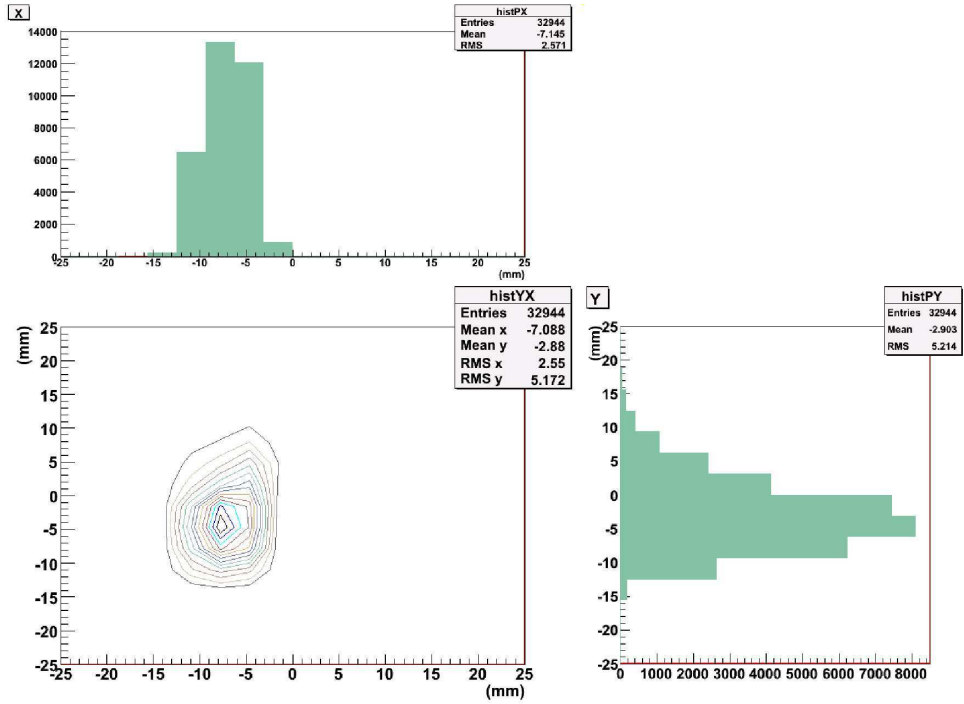


Figure B.8: Collimator in up orientation, final slits, source moved 2mm up

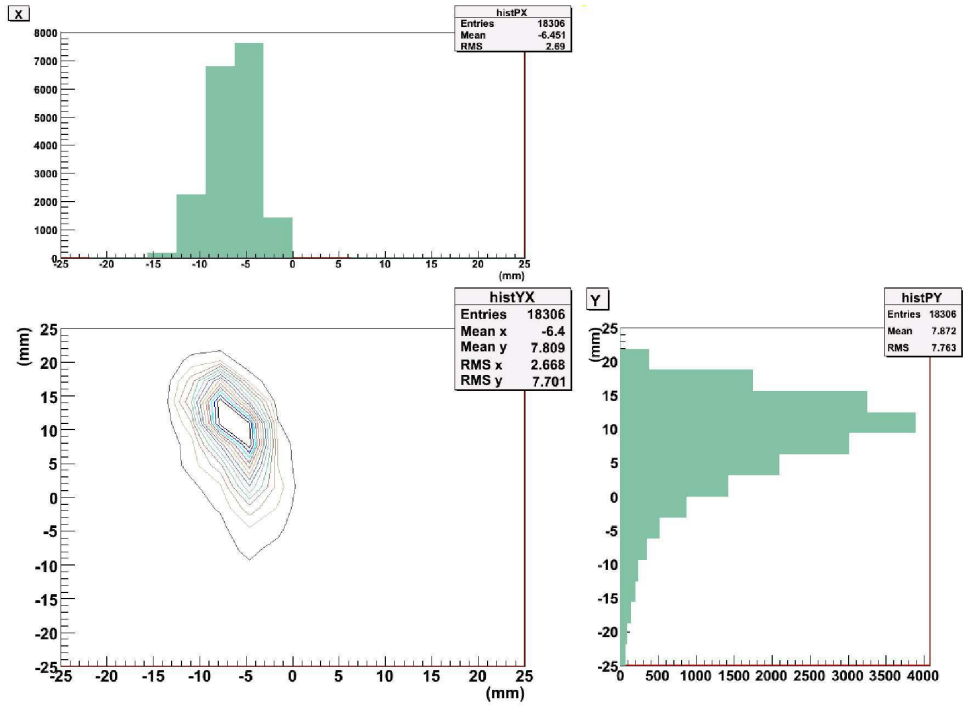


Figure B.9: Collimator in down orientation, final slits, source moved 2mm up

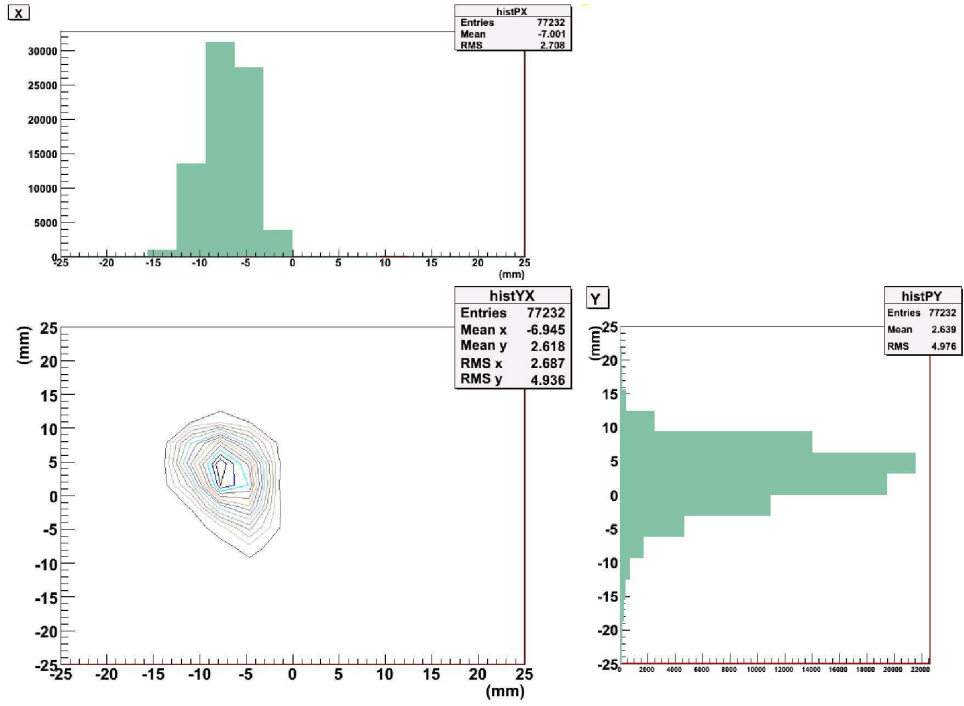


Figure B.10: Collimator in hole orientation, final slits, source moved 2mm up

APPENDIX C

MAGNETIC AND ELECTRIC FIELD SETTINGS

MD1 was set for an energy of 3.15 Mev, atomic mass of 4.0, and charge of 2+, the magnetic field reading for MD1 was 2561.4 G. All quadrupoles and the other MD magnetic fields are given as ratios to that of MD1 and are shown in Table C.1.

Sextupoles are controls by current rather than magnetic field, Table C.2 gives current ratios of the sextupole elements with respect to MD1.

The electric dipoles were set to 81.5 kV (ED1) and 63.5 kV (ED2) unless otherwise stated.

Element	Ratio of B-field (to MD1)
Q1	0.709
Q2	0.674
MD1	1.000
Q3	0.552
Q4	0.732
Q5	0.380
Q6	0.365
Q7	0.510
MD2	1.226
Q8	0.387
Q9	0.236
Q10	0.264

Table C.1: Magnetic Field Ratios for Quadrupoles

Element	Ratio of current (to MD1)
S1	0.0527
MD1	1.000
S2	0.0114
S3	0.00900
S4	0.0.0960

Table C.2: Current Ratios for Sextupoles

BIBLIOGRAPHY

- [1] Aaron Bebington. Enter The DRAGON: Investigating the $^{13}\text{C}(p,\gamma)^{14}\text{N}$ reaction .
<http://dragon.triumf.ca/docs/aaron-report.pdf>.
- [2] CERN. GEANT. <http://wwwasd.web.cern.ch/wwwasd/geant/>.
- [3] J. M. D'Auria, R. E. Azuma, S. Bishop, L. Buchmann, M. L. Chatterjee, A. A. Chen, S. Engel, D. Gigliotti, U. Greife, D. Hunter, A. Hussein, D. Hutcheon, C. C. Jewett, J. José, J. D. King, A. M. Laird, M. Lamey, R. Lewis, W. Liu, A. Olin, D. Ottewell, P. Parker, J. Rogers, C. Ruiz, M. Trinczek, and C. Wrede. The $^{21}\text{Na}(p,\gamma)^{22}\text{Mg}$ reaction from $E_{c.m.} = 200$ to 1103 keV in novae and x-ray bursts. *Phys. Rev. C.*, 69(6):065803—+, June 2004.
- [4] Dragon. Dragon Gas Target Logbook.
- [5] J.-U. Ness, S. Starrfield, J. J. Drake, M. Orio, M. F. Bode, T. J. O'Brien, R. J. Davis, J. Osborne, K. L. Page, G. Schwarz, J. Krautter, A. Evans, S. P. S. Eyres, R. Gehrz, and C. Woodward. RS Ophiuchi. *IAUC*, 8683:2—+, March 2006.
- [6] J. Pearson. Testing Dragon's Acceptance.
- [7] C. E. Rolfs and W. S. Rodney. *Cauldrons in the cosmos: Nuclear astrophysics*. Research supported by NSF, Georgetown University, DFG, et al. Chicago, IL, University of Chicago Press, 1988, 579 p., 1988.
- [8] W. K. Rose. *Advanced Stellar Astrophysics*. Cambridge University Press, 1998.

-
- [9] C. Ruiz, A. Parikh, J. José, L. Buchmann, J. A. Caggiano, A. A. Chen, J. A. Clark, H. Crawford, B. Davids, J. M. D'Auria, C. Davis, C. Deibel, L. Erikson, L. Fogarty, D. Frekers, U. Greife, A. Hussein, D. A. Hutcheon, M. Huyse, C. Jewett, A. M. Laird, R. Lewis, P. Mumby-Croft, A. Olin, D. F. Ottewell, C. V. Ouellet, P. Parker, J. Pearson, G. Ruprecht, M. Trinczek, C. Vockenhuber, and C. Wrede. Measurement of the $E_{c.m.}=184\text{keV}$ Resonance Strength in the $^{26}\text{gAl}(p,\gamma)^{27}\text{Si}$ Reaction. *Physical Review Letters*, 96(25):252501–+, June 2006.
- [10] Josh Slater. GEANT Simulations of DRAGON and the $^{12}\text{C}(^{12}\text{C},\gamma)^{24}\text{Mg}$ Reaction. <http://dragon.triumf.ca/docs/joshreport.pdf>.
- [11] J. Zylberberg, D. Hutcheon, L. Buchmann, J. Caggiano, A. Hussein, E. O'Connor, D. Ottewell, C. Ruiz, M. Trinczek, and C. Vockenhuber. Charge-State Distributions after Radiative Capture. *Nucl. Instr. and Meth B*, submitted, 2006.